CHALMERS

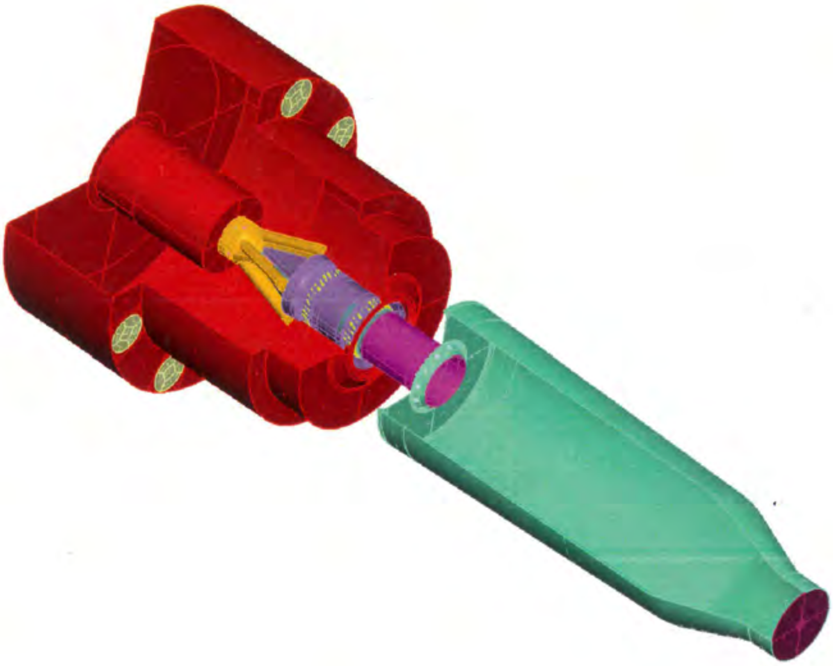

Flow simulations of a gas turbine burner using CFX and OpenFOAM

Master's Thesis in Solid and Fluid Mechanics

ERIK LARSSON

Department of Applied Mechanics
Division of Fluid Dynamics
CHALMERS UNIVERSITY OF TECHNOLOGY
Göteborg, Sweden 2009
Master's Thesis 2009:07

MASTER'S THESIS 2009:07

Flow simulations of a gas turbine burner using CFX and OpenFOAM

Master's Thesis in Solid and Fluid Mechanics
ERIK LARSSON

Department of Applied Mechanics
Division of Fluid Dynamics
CHALMERS UNIVERSITY OF TECHNOLOGY

Göteborg, Sweden 2009

Flow simulations of a gas turbine burner using CFX and OpenFOAM
ERIK LARSSON

Master's Thesis 2009:07
ISSN 1652-8557
Department of Applied Mechanics
Division of Fluid Dynamics
Chalmers University of Technology
SE-412 96 Göteborg
Sweden
Telephone: + 46 (0)31-772 1000

Cover:
Third generation dry low emissions burner.

Chalmers Reproservice
Göteborg, Sweden 2009

Flow simulations of a gas turbine burner using CFX and OpenFOAM
Master's Thesis in Solid and Fluid Mechanics
ERIK LARSSON
Department of Applied Mechanics
Division of Fluid Dynamics
Chalmers University of Technology

Abstract

In this thesis, simulations of a water test rig for gas turbine burners have been performed. The burner in the study has been a third generation dry low emissions burner from Siemens. The simulations have been performed with both the commercial software, CFX and the open source software OpenFOAM. The aim of the thesis has been to evaluate the performance of OpenFOAM. The results from the simulations show that there are some differences between OpenFOAM and CFX.

Keywords: CFD OpenFOAM CFX Gas turbine burner

Contents

Acknowledgements

I would like to take the opportunity to thank people who made this thesis work possible.

First I would like to thank Dr. Jonas Bredberg at Epsilon, the supervisor for my thesis work. He has been of great support and without his guidance, this thesis would not be possible.

Furthermore, Dr. Daniel Lörstad at Siemens Industrial Turbomachinary AB in Finspång has been of great help. He has not only supplied me with vital input data but has also given me constructive criticism and helped me to improve the thesis.

Adj. Prof. Christer Fureby also gave me some valuable input and helped me move forward with the thesis.

I would like to thank Prof. Lars Davidson for being the examiner for my thesis work.

Last but not least I would like to thank friends and family for their loving support.

Göteborg June 2009
Erik Larsson

1 Introduction

In this chapter some background information is presented that will help the reader to put this thesis in its proper context.

1.1 Purpose

The purpose of this project is to evaluate the performance of the open source software OpenFOAM with aspect to both the commercial software CFX and experimental data. The purpose is also to evaluate what method of simulation is needed to accurately simulate the flow. The case in question is the flow through a Siemens third generation dry low emissions burner in the water test rig.

1.2 Method

The method used in this project is to go through all three stages of numerical simulations, pre- processing, solving and post- processing. The mesh generation of the computational domain is included in the pre- processing.

1.3 Limitations

The experimental data are taken at face value, assuming that the data have been both correctly sampled and post processed. Neither have the CFX code been altered.

1.4 Siemens

Siemens is a multi national company with a vast range of products and services. Among them are gas turbine solutions for power generation. Gas turbines are manufactured by Siemens in the range between 5 and 340 MW [5].

1.5 Gas Turbines

Gas turbines are used in many applications. Gas turbines are split in two main subcategories, aero engines and stationary gas turbines. Both kinds of gas turbines consist of three main parts, a compressor, a combustor and a turbine. The three main parts can be seen in figure 1.1.

The compressor compresses air before the air is mixed with fuel in the burner and combusted in the combustion chamber. The hot gas is then expanded in the turbine section. The main difference between the two kinds are that stationary gas turbines can be made sturdier for longer service life and that the gas velocity at the exhaust is a loss for stationary turbines.

1.6 Gas Turbine Burners

Gas turbine burners are a part of the combustor. The burner mixes compressed air and fuel before the mixture is combusted in the combustion chamber. Industrial gas turbines can use both gaseous and liquid fuel as the source of energy. The most common fuel is natural gas with diesel as the second most common.

The mixing between the air and the fuel is crucial to obtain an even combustion process and limits the problems that occurs when the fuel distribution in the burner is uneven, such as increased NO_x, CO and unburnt hydrocarbons emissions. Mixing problems in burners

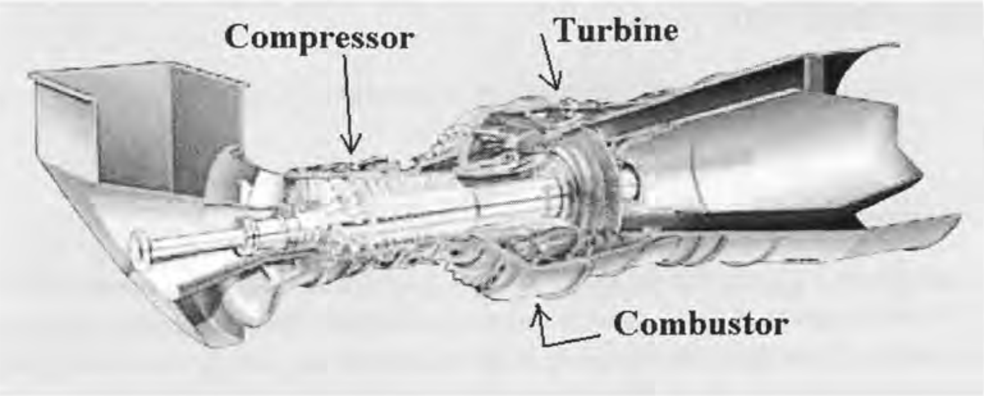

Figure 1.1: Siemens gas turbine SGT- 800.

also lead to flashbacks and pulsations, for which a security system is needed. Uneven fuel distribution between different burners lead to different flame temperature and exposes the turbine and combustion chamber to heavier wear.

1.7 Computational Fluid Dynamics Codes

OpenFOAM was chosen as a software because it is open source. The OpenFOAM version 1.5-development, was used in the work. The choice of CFX as the commercial code to compare with OpenFOAM, was because it is currently at use at Siemens Industrial Turbomachineray in Finspång. CFX is a product of Ansys Inc.

2 Theory

In this chapter, the basic theory for fluid motion is presented briefly. Firstly the governing equations are derived and secondly, some numerical models of the governing equations are presented. The governing equations defines the conservation of mass, momentum and energy of a fluid element.

2.1 Navier-Stokes

The governing equations for fluid motion are called the Navier-Stokes equations after Claude-Louis Navier and George Gabriel Stokes. The basic principle is to apply the conservation of mass, momentum and energy to a fluid element. A fluid element is any thermodynamic system where the physical properties are considered to be constant. A fluid element is large enough to average over a large number of molecules so that the continuum hypothesis is applicable.

2.1.1 Conservation of mass

The conservation of mass, or the continuity equation, states that the amount of mass that flows in to any fixed volume must be balanced by the amount of mass that flows out of the volume. The mass flux through a surface of a fluid element is equal to the mass transport at the centre of the fluid element plus the change in mass flux that takes place at the distance between the centre and the face. A fluid element with the mass flux at all the six faces can be seen in figure 2.1.

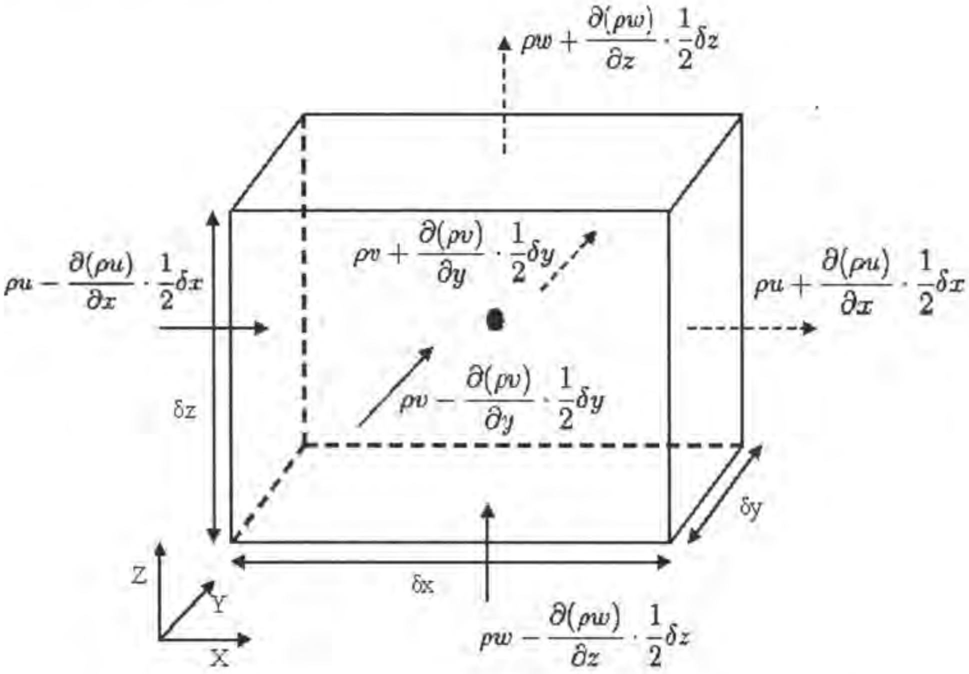

Figure 2.1: Fluid element with mass flux through the surfaces.

The equation of the conservation of mass can then be written as:

$$
\begin{aligned}
&(\rho u - \frac{\partial(\rho u)}{\partial x}\cdot\frac{1}{2}\delta x)\delta y\delta z - (\rho u + \frac{\partial(\rho u)}{\partial x}\cdot\frac{1}{2}\delta x)\delta y\delta z\\
&+(\rho v - \frac{\partial(\rho v)}{\partial y}\cdot\frac{1}{2}\delta y)\delta x\delta z - (\rho v + \frac{\partial(\rho v)}{\partial y}\cdot\frac{1}{2}\delta y)\delta x\delta z\\
&+(\rho w - \frac{\partial(\rho w)}{\partial z}\cdot\frac{1}{2}\delta z)\delta x\delta y - (\rho w + \frac{\partial(\rho w)}{\partial z}\cdot\frac{1}{2}\delta z)\delta x\delta y = 0
\end{aligned}
\tag{2.1}
$$

After summation and division with the fluid volume, $\delta V = \delta x\delta y\delta z$, the equation is given as:

$$\frac{\partial(\rho u)}{\partial x} + \frac{\partial(\rho v)}{\partial y} + \frac{\partial(\rho w)}{\partial z} = 0 \tag{2.2}$$

The rate of change of mass in time can be written as:

$$\frac{\partial \rho\delta x\delta y\delta z}{\partial t} = \frac{\partial \rho}{\partial t}\delta x\delta y\delta z \tag{2.3}$$

After combining equation 2.2 and 2.3 the complete continuity equation is given:

$$\frac{\partial \rho}{\partial t} + \frac{\partial(\rho u)}{\partial x} + \frac{\partial(\rho v)}{\partial y} + \frac{\partial(\rho w)}{\partial z} = 0 \tag{2.4}$$

2.1.2 Conservation of momentum

The conservation of momentum is derived by applying Newton's second law, i.e. the sum of all forces are equal to the mass times the acceleration, on a fluid element. First therefore the forces on a fluid element are identified and shown in figure 2.2 .

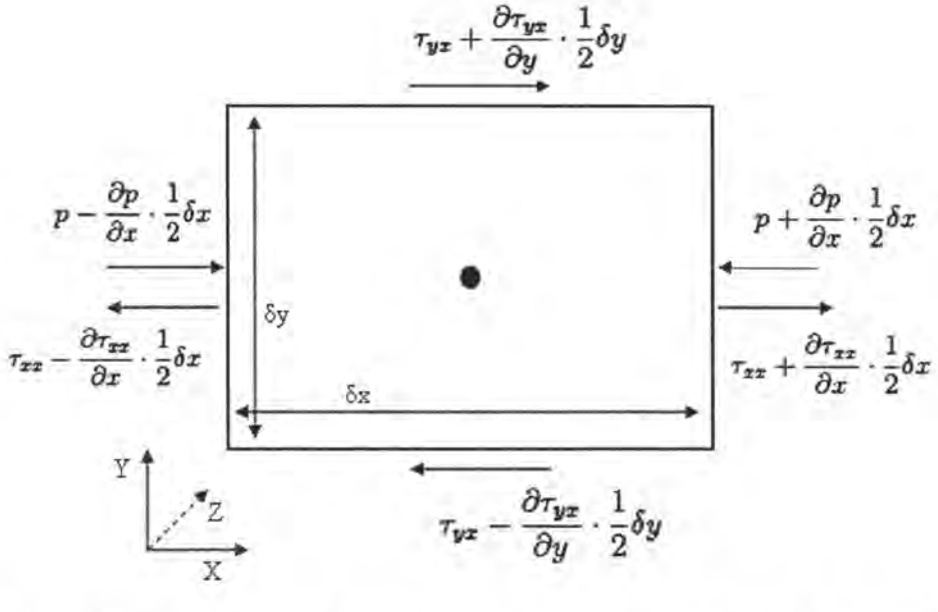

Figure 2.2: Fluid element with surface stresses in x-direction shown for two dimensions.

The element body forces in x-direction that arise from e.g. gravity are gathered in a single term, S_x.

The momentum equation in x-direction can then, in all three dimensions, be written as:

$$\begin{aligned} m\frac{Du}{Dt} &= (\tau_{xx} + \frac{\partial \tau_{xx}}{\partial x} \cdot \frac{1}{2}\delta x)\delta y \delta z - (\tau_{xx} - \frac{\partial \tau_{xx}}{\partial x} \cdot \frac{1}{2}\delta x)\delta y \delta z \\ &+ (\tau_{yx} + \frac{\partial \tau_{yx}}{\partial y} \cdot \frac{1}{2}\delta y)\delta x \delta z - (\tau_{yx} - \frac{\partial \tau_{yx}}{\partial y} \cdot \frac{1}{2}\delta y)\delta x \delta z \\ &+ (\tau_{zx} + \frac{\partial \tau_{zx}}{\partial z} \cdot \frac{1}{2}\delta z)\delta x \delta y - (\tau_{zx} - \frac{\partial \tau_{zx}}{\partial z} \cdot \frac{1}{2}\delta z)\delta x \delta y \\ &+ (p - \frac{\partial p}{\partial x} \cdot \frac{1}{2}\delta x)\delta y \delta z - (p + \frac{\partial p}{\partial x} \cdot \frac{1}{2}\delta x)\delta y \delta z + S_x \delta x \delta y \delta z \end{aligned} \tag{2.5}$$

In the equation above the total momentum change or material derivative,

$$m\frac{Du}{Dt} = m\left(\frac{\partial u}{\partial t} + u\frac{\partial u}{\partial x} + v\frac{\partial u}{\partial y} + w\frac{\partial u}{\partial z}\right) \tag{2.6}$$

includes the rate of momentum change in both time and space. Simplifying equation 2.5 and dividing by the element volume $\delta x \delta y \delta z$ gives:

$$\rho\frac{Du}{Dt} = \frac{\partial \tau_{xx}}{\partial x} + \frac{\partial \tau_{yx}}{\partial y} + \frac{\partial \tau_{zx}}{\partial z} - \frac{\partial p}{\partial x} + S_x \tag{2.7}$$

The same equation can then be derived in the same way for both the y- and z-directions. The equations analogous with equation 2.7 then becomes:

$$\rho\frac{Dv}{Dt} = \frac{\partial \tau_{xy}}{\partial x} + \frac{\partial \tau_{yy}}{\partial y} + \frac{\partial \tau_{zy}}{\partial z} - \frac{\partial p}{\partial y} + S_y \tag{2.8}$$

$$\rho\frac{Dw}{Dt} = \frac{\partial \tau_{xz}}{\partial x} + \frac{\partial \tau_{yz}}{\partial y} + \frac{\partial \tau_{zz}}{\partial z} - \frac{\partial p}{\partial z} + S_z \tag{2.9}$$

Using Einstein summation index, the three dimensional momentum equations are written:

$$\rho\frac{Du_i}{Dt} = \frac{\partial \tau_{ij}}{\partial x_j} - \frac{\partial p}{\partial x_i} + S_i \tag{2.10}$$

The stress tensor τ_{ij}, is often modelled assuming a Newtonian fluid. A Newtonian fluid is a fluid where the rate of deformation is proportional to the shear stress. If the fluid is assumed to be isotropic and incompressible there is only a single constant of proportionality, the dynamic viscosity, μ. For a Newtonian incompressible fluid the stress tensor is modelled as:

$$\tau_{ij} = \mu\left(\frac{\partial u_i}{\partial x_j} + \frac{\partial u_j}{\partial x_i}\right) \tag{2.11}$$

Using this assumption and the continuity equation for incompressible flow, $\partial u_i/\partial x_i = 0$, the formulation of the momentum equation known as Navier- Stokes equations is obtained:

$$\rho\frac{Du_i}{Dt} = -\frac{\partial p}{\partial x_i} + \frac{\partial}{\partial x_j}\left(\mu\frac{\partial u_i}{\partial x_j}\right) + S_i \tag{2.12}$$

2.1.3 Conservation of energy

The rate of energy change is equal to the work done by the system plus the heat transferred to the system according to the first law of thermodynamics. The total rate of change of energy is written as:

$$\rho \frac{DE}{Dt} \tag{2.13}$$

where, as in equation 2.6, the material derivative has been used.

For the work done by the system, the surface forces are once again identified. To obtain the work done by these forces they are multiplied with the velocity. For a graphical description of the surface forces in x- direction in two dimensions, see figure 2.2. Summing the forces in all three dimensions and multiplying each force with the velocity, the work done in x- direction by the element is written as:

$$\begin{aligned}
&(\tau_{xx}u + \frac{\partial \tau_{xx}u}{\partial x} \cdot \frac{1}{2}\delta x)\delta y \delta z - (\tau_{xx}u - \frac{\partial \tau_{xx}u}{\partial x} \cdot \frac{1}{2}\delta x)\delta y \delta z \\
&+(\tau_{yx}u + \frac{\partial \tau_{yx}u}{\partial y} \cdot \frac{1}{2}\delta y)\delta x \delta z - (\tau_{yx}u - \frac{\partial \tau_{yx}u}{\partial y} \cdot \frac{1}{2}\delta y)\delta x \delta z \\
&+(\tau_{zx}u + \frac{\partial \tau_{zx}u}{\partial z} \cdot \frac{1}{2}\delta z)\delta x \delta y - (\tau_{zx}u - \frac{\partial \tau_{zx}u}{\partial z} \cdot \frac{1}{2}\delta z)\delta x \delta y \\
&+(pu - \frac{\partial pu}{\partial x} \cdot \frac{1}{2}\delta x)\delta y \delta z - (pu + \frac{\partial pu}{\partial x} \cdot \frac{1}{2}\delta x)\delta y \delta z
\end{aligned} \tag{2.14}$$

Simplification of equation 2.14 and division with the fluid element volume, $\delta x \delta y \delta z$, gives:

$$\frac{\partial \tau_{xx}u}{\partial x} + \frac{\partial \tau_{yx}u}{\partial y} + \frac{\partial \tau_{zx}u}{\partial z} - \frac{\partial pu}{\partial x} \tag{2.15}$$

The work done by the surface forces in y- and z- direction can, analogous with the equation in x- direction, be written as:

$$\frac{\partial \tau_{xy}v}{\partial x} + \frac{\partial \tau_{yy}v}{\partial y} + \frac{\partial \tau_{zy}v}{\partial z} - \frac{\partial pv}{\partial y} \tag{2.16}$$

$$\frac{\partial \tau_{xz}w}{\partial x} + \frac{\partial \tau_{yz}w}{\partial y} + \frac{\partial \tau_{zz}w}{\partial z} - \frac{\partial pw}{\partial z} \tag{2.17}$$

Using Einstein summation index, the work done in three dimensions is written:

$$\frac{\partial \tau_{ji}u_i}{\partial x_j} - \frac{\partial pu_i}{\partial x_i} \tag{2.18}$$

The heat transferred to the system is described by a heat flux vector, q_i. The flux through each surface on a fluid element can be seen in figure 2.3 .

A heat flux balance can be established as:

$$\begin{aligned}
&(q_x - \frac{\partial q_x}{\partial x} \cdot \frac{1}{2}\delta x)\delta y \delta z - (q_x + \frac{\partial q_x}{\partial x} \cdot \frac{1}{2}\delta x)\delta y \delta z \\
&+(q_y - \frac{\partial q_y}{\partial y} \cdot \frac{1}{2}\delta y)\delta x \delta z - (q_y + \frac{\partial q_y}{\partial y} \cdot \frac{1}{2}\delta y)\delta x \delta z \\
&+(q_z - \frac{\partial q_z}{\partial z} \cdot \frac{1}{2}\delta z)\delta x \delta y - (q_z + \frac{\partial q_z}{\partial z} \cdot \frac{1}{2}\delta z)\delta x \delta y
\end{aligned} \tag{2.19}$$

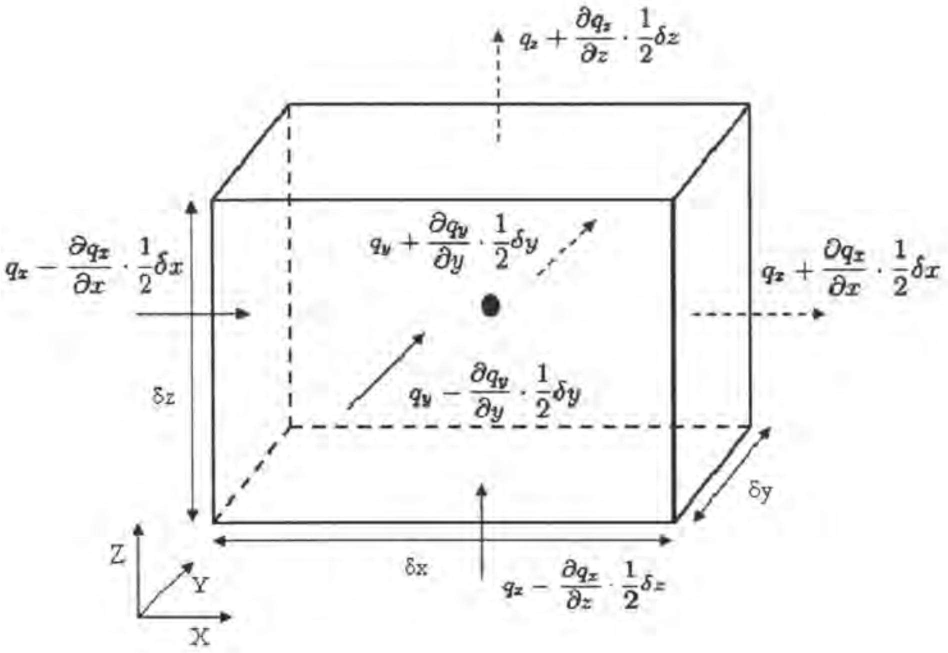

Figure 2.3: Fluid element with surface heat flux.

Again simplification and division with the fluid element volume gives:

$$-\frac{\partial q_x}{\partial x} - \frac{\partial q_y}{\partial y} - \frac{\partial q_z}{\partial z} \tag{2.20}$$

The heat flux vector is related to temperature by Fourier's law of heat conduction. If the fluid is assumed to be isotropic, the heat flux can be written:

$$q_x = -k\frac{\partial T}{\partial x} \tag{2.21}$$

where k is the thermal conductivity.

Using this relation on equation 2.20 above, the equation is written:

$$-\frac{\partial}{\partial x}\left(-k\frac{\partial T}{\partial x}\right) - \frac{\partial}{\partial y}\left(-k\frac{\partial T}{\partial y}\right) - \frac{\partial}{\partial z}\left(-k\frac{\partial T}{\partial z}\right) \tag{2.22}$$

Returning to the first law of thermodynamics, the energy equation in three dimensions, where a source term S_E has been added, is written:

$$\rho\frac{DE}{Dt} = \frac{\partial \tau_{ji}u_i}{\partial x_j} - \frac{\partial p u_i}{\partial x_i} + \frac{\partial}{\partial x_i}\left(k\frac{\partial T}{\partial x_i}\right) + S_E \tag{2.23}$$

2.1.4 Scalar transport

The rate of change of the concentration of a scalar in a cell is changed in two ways, convection and diffusion. The equation for the change of concentration of a scalar is written

$$\rho\frac{Dc}{Dt} = \Gamma\frac{\partial c}{\partial x_j} \tag{2.24}$$

where c is the scalar concentration and Γ is the diffusion coefficient.

The scalar concentration can be interpreted as the concentration of anything that does not change the flow. Concern needs to be taken to any mechanism, e.g. reaction, that change the total mass of the specie in question.

2.1.5 Reynolds averaging

The equations in sections 2.1.1 - 2.1.4 all contain the instantaneous values of the variables. The values can be divided into a fluctuating part and a time averaged mean part, this is known as Reynolds decomposition.

$$\phi = \Phi + \phi' \tag{2.25}$$

The averaged value of any variable, Φ, of the instantaneous value of the variable, ϕ is defined as:

$$\Phi = \frac{1}{\Delta t}\int_0^{\Delta t} \phi \, dt = \overline{\phi} \tag{2.26}$$

The mean and fluctuating properties also have the following characteristics. Any average of a fluctuating variable is zero, eq 2.27. Any average of an average value is the same average value, eq 2.28. The averaged value of a product of a time averaged value and a fluctuating value is zero, eq 2.29. Finally, one of the properties is that an average of the product of two fluctuating variables is zero only if the variables are independent of each other.

$$\overline{\phi'} = 0 \tag{2.27}$$

$$\overline{\Phi} = \Phi \tag{2.28}$$

$$\overline{\Phi\phi'} = 0 \tag{2.29}$$

By applying the decomposition to the momentum equations, eq. 2.12 the following equations are obtained:

$$\rho\frac{D(U_i + u'_i)}{Dt} = -\frac{\partial(P + p')}{\partial x_i} + \mu\frac{\partial}{\partial x_j}\left(\frac{\partial(U_i + u'_i)}{\partial x_j} + \frac{\partial(U_j + u'_j)}{\partial x_i}\right) + S_i \tag{2.30}$$

By taking the time average of the decomposed equations, the result is the Reynolds averaged Navier Stokes (RANS) as follows:

$$\rho\frac{DU_i}{Dt} = -\frac{\partial P}{\partial x_i} + \mu\frac{\partial}{\partial x_j}\left(\frac{\partial U_i}{\partial x_j}\right) - \rho\frac{\partial\overline{u'_iu'_j}}{\partial x_j} + S_i \tag{2.31}$$

The additional term that occurs in the equation, $-\rho\frac{\partial\overline{u'_iu'_j}}{\partial x_j}$, contains the product of the fluctuating velocities, $\overline{u'_iu'_j}$. Since the term behaves much like the viscous stress term, they are known as the Reynolds stresses.

2.1.6 Closure problems

In the sections 2.1.1 - 2.1.3, there are one equation for the conservation of mass, three equations for the conservation of momentum and one equation for the conservation of energy, five governing equations in all.

Unfortunately there are three unknown velocities, one unknown pressure, one unknown total energy, three unknown heat fluxes and nine unknown surface stresses, 17 unknowns in all. With the assumptions of Newtonian fluids and Fourier's law of heat conduction, the nine unknown surface stresses and three unknown heat fluxes are reduced to an unknown temperature and two modelling constants. This reduces the number of unknowns to six, velocities, pressure, temperature and total energy. The system of equations above is still not possible to solve. If an equation of state is added for the fluid, e.g. the perfect gas law, the pressure is a function of density and temperature, the number of unknowns is dropped to five and the system of equations is closed as long as the necessary initial and boundary conditions are supplied.

However, when we consider the fluctuating velocities and the Reynolds stresses that were introduced in section 2.1.5, there are more unknowns. Since the Reynolds stress tensor is symmetric there are six more unknowns, $\overline{u'_x u'_x}$, $\overline{u'_x u'_y}$, $\overline{u'_x u'_z}$, $\overline{u'_y u'_y}$, $\overline{u'_y u'_z}$ and $\overline{u'_z u'_z}$. The total number of unknowns are eleven for a general case and ten for incompressible flows where the density can be considered to be constant. The number of equations are still five which means that the system is undetermined.

2.2 Turbulence

Turbulence is rapid, unsteady and nonlinear movement of fluids occurring in three dimensions at a diversity of length and time scales. Turbulent flow is always difficult to predict but the calculations and predictions of them are important nonetheless.

2.2.1 Models

Solving the governing equations directly is in most cases not feasible. Hence, the need for numerical models of the governing equations is apparent. The drawback of all models is that you lose the details that will predict the unsteadiness and nonlinearities of the flow.

Numerical models go hand in hand with experimental studies. Numerical modelling has to be validated with experiments since numerical models are limited in their accuracy. On the other hand numerical simulations are often cheaper than experiments and offer a greater flexibility than experiments. In most cases you are also restricted to a number of possible measurements in any given experiment, something that you want to know can not always easily be measured.

Common for all attempts of modelling is to achieve high accuracy and high stability at a low computational cost. There is always a trade of between these three goals.

Zero equation models

A common way of modelling the Reynolds stresses is to use the Boussinesq assumption. The Boussinesq assumption states that the Reynolds stresses are proportional to the traceless viscous stress tensor with a proportionality constant, μ_t.

$$-\rho\overline{u'_i u'_j} = \mu_t\left(\frac{\partial U_i}{\partial x_j} + \frac{\partial U_j}{\partial x_i}\right) - \frac{2}{3}\rho k \delta_{ij} \tag{2.32}$$

δ_{ij} is the Kronecker delta and $k = \frac{1}{2}(u'^2 + v'^2 + w'^2)$ is the turbulence kinetic energy. μ_t is referred to as the eddy viscosity and is a property of the flow, not the fluid.

The Boussinesq assumption relates the fluctuating velocities to the mean velocities of the flow. Considering the closure problem in section 2.1.6 the question of finding the Reynolds stresses is now replaced by the question of finding a model for the eddy viscosity.

One such attempt to model the eddy viscosity is to use Prandtl's mixing length model. The mixing length model is derived from dimensional analysis. The dimension of the eddy viscosity is [Pa s] and with dimensional analysis we find that:

$$\mu_t = C\rho\ell\vartheta \tag{2.33}$$

where C is a proportionality constant, ρ is the density, $\ell[L]$ is a turbulence length scale and $\vartheta\left[\frac{L}{T}\right]$ is a turbulence velocity scale. The largest eddies of the flow contain more kinetic energy than the smaller eddies and will therefore effect the mean velocities of the flow the most. A suitable length scale would be the diameter of the eddies. The turbulence velocity scale is a little less straight forward. According to Prandtl's mixing length model it can be estimated with the mixing length times the largest velocity derivative. This will introduce a new proportionality constant that can be absorbed, together with C, into a modified length scale, ℓ_m. ℓ_m can be found in tables for a variety of flows.

One equation models

In a one equation model the Boussinesq assumption is still used and the problem is again to find the eddy viscosity, μ_t, to describe our flow. In a one equation model the eddy viscosity is modelled with:

$$\mu_t = \rho\ell\sqrt{k} \tag{2.34}$$

where a transport equation is solved for k. The dissipation of kinetic energy is assumed to be proportional to the kinetic energy and expressed as:

$$\epsilon = \frac{C_D k^{3/2}}{\ell} \tag{2.35}$$

This assumption and the Boussinesq assumption is used to formulate a kinetic energy equation. See section 3.2 for a further discussion on this kinetic energy equation.

Two equation models

As in the one equation models, the Boussinesq assumption about the relationship between Reynolds stresses is used. And again there is the eddy viscosity, μ_t, that we need to model. The idea in the two equation models is to calculate μ_t with some turbulence quantities for which a transport equation can be formulated.

The most common two equation model is the $k-\epsilon$ model. The two turbulence quantities that are used in calculating μ_t are the turbulence kinetic energy, k, and the dissipation of kinetic energy, ϵ. The dimensional analysis with $k\left[\frac{L^2}{T^2}\right]$ and $\epsilon\left[\frac{L^2}{T^3}\right]$ gives:

$$\mu_t = C\rho\frac{k^2}{\epsilon} \tag{2.36}$$

To solve a transport equation means that the production, dissipation and diffusion of the turbulence quantity are modelled. The k and ϵ equations are derived from the instantaneous Navier- Stokes equations. The k equation is derived by multiplying the momentum equation with the fluctuating velocity vector, the momentum equation in x-direction will be multiplied with u, the fluctuating velocity in x- direction. In the same way, the velocities in y- and z- direction will be multiplied with its corresponding velocity. The trace of the matrix will then give the turbulence kinetic energy. After Reynolds decomposition of the instantaneous properties, u and p, some rearranging and identification of the turbulence kinetic energy, $k = \frac{1}{2}(u'^2 + v'^2 + w'^2)$, the following equation is the result:

$$\rho\frac{Dk}{Dt} = \frac{\partial}{\partial x_j}\left(-\overline{p'u'_j} + 2\mu\overline{u'_i s'_{ij}} - \rho\overline{u'_i u'_i u'_j}\right) - 2\mu\overline{s'_{ij}s'_{ij}} - \rho\overline{u'_i u'_j}S_{ij} \tag{2.37}$$

The fact that the tensor $\frac{\partial u_i}{\partial x_j}$ can be written in a symmetric, and a anti- symmetric part have been used.

$$\frac{\partial u_i}{\partial x_j} = \omega_{ij} + s_{ij} \tag{2.38}$$

where $\omega_{ij} = \frac{1}{2}\left(\frac{\partial u_i}{\partial x_j} - \frac{\partial u_j}{\partial x_i}\right)$ is the anti- symmetric part and $s_{ij} = \frac{1}{2}\left(\frac{\partial u_i}{\partial x_j} + \frac{\partial u_j}{\partial x_i}\right)$ is the symmetric part referred to as the strain rate tensor. The models are formulated in section 3.2.

Reynolds stress model

Since the Reynolds stresses are causing problems in the RANS, eq. 2.31, a transport equation for the Reynolds stresses would be better than a single equation for all of the stresses. A transport model for the Reynold stresses is derived by first finding an equation for the fluctuating velocities. This one is obtained by subtracting the RANS equations, eq. 2.31 from the decomposed Navier-Stokes, eq. 2.30. The result of this operation is

$$\rho\frac{Du'_i}{Dt} = \frac{\partial p'}{\partial x_i} + \frac{\partial}{\partial x_j}\mu\left(\frac{\partial u'_i}{\partial x_j}\right) - \rho u'_j\frac{\partial U_i}{\partial x_i} - u'_j\frac{\partial u'_i}{\partial x_i} + \rho\frac{\partial\overline{u'_i u'_j}}{\partial x_j} \tag{2.39}$$

By multiplying this equation with the fluctuating velocity vector u'_k there are one equation with two independent indices, i and k. It is therefore possible to switch the indices and the two equations together to obtain the Reynolds stress equation, which can after a fair amount of reordering be written:

$$\begin{aligned}\rho\frac{D\overline{u_i u_k}}{Dt} &= \overline{-p\left[\frac{\partial u_i}{\partial x_k} + \frac{\partial u_k}{\partial x_i}\right]}\\ &\quad + \frac{\partial}{\partial x_j}\left\{-\rho[\overline{pu_k}\delta_{ij} + \overline{pu_i}\delta_{kj}] - \rho\overline{u_i u_k u_j} + 2\mu[\overline{s_{ij}u_k} + \overline{s_{ij}u_k}]\right\}\\ &\quad - \rho\left[\overline{u_i u_j}\frac{\partial U_k}{\partial x_j} + \overline{u_k u_j}\frac{\partial U_i}{\partial x_j}\right] - 2\mu\left[\overline{s_{ij}\frac{\partial u_k}{\partial x_j}} + \overline{s_{kj}\frac{\partial u_i}{\partial x_j}}\right]\end{aligned} \tag{2.40}$$

In equation 2.40 it is necessary to model all the different terms except for the production term, $\rho\left[\overline{u_i u_j}\frac{\partial U_k}{\partial x_j} + \overline{u_k u_j}\frac{\partial U_i}{\partial x_j}\right]$, since the Reynold stresses are solved for and the mean velocities are known from the momentum equations.

2.2.2 Direct numerical simulations and large eddy simulations

Of course the most obvious way to do simulations is to use the closed equation system of three momentum equations and the continuity equation to solve for the instantaneous velocities and pressure. This is called direct numerical simulation (DNS) and means that the turbulent eddies at the smallest scales of motion and time are resolved. This leads to a very fine grid and time resolution. In order to resolve the eddies in space, the grid size needs to approach the Kolmogorov micro scale, $\eta_K = \left(\frac{\nu^3}{\epsilon}\right)^{\frac{1}{4}}$, which is the smallest scale of motion for a flow. The resolution in time is determined by the Courant, Friedirch and Levy (CFL) number, $\Delta t = CFL\Delta x/|u|$. The CFL number must be less than one in order to ensure full time resolution.

Let us assume that turbulent eddies behave much the same at the smallest scales regardless of the mean flow. Dividing the flow in two parts, bigger eddies where the flow is resolved and smaller eddies where the flow is modelled, would escape one of the major drawbacks of RANS simulations where all the eddies are modelled in the same way. This way of doing simulations is called Large eddy simulation (LES).

The large scales are limited in size by the computational domain, the size of the grid determines how small scales it is possible to solve for. The flow that occurs at scales smaller than the computational grid will have to be modelled, and the model for the smaller eddies are therefore referred to as a subgrid scales (SGS) model. To achieve this division of scales a filter is introduced.

The filter in one dimension is defined as:

$$\overline{u}(x) = \int_{-\infty}^{\infty} G(r)u(x-r)\,dr \tag{2.41}$$

$$\int_{-\infty}^{\infty} G(r)\,dr = 1 \tag{2.42}$$

In the spectral space there is a cut off wavenumber, $\kappa_c = \pi/\Delta$ which makes the Fourier transformed filtering function cut off all the wavenumbers above κ_c.

$$\hat{G}(\kappa) = \begin{cases} 1 & \text{if } \kappa \leq \kappa_c \\ 0 & \text{otherwise} \end{cases} \tag{2.43}$$

There is also a box filter in LES where the equations are filtered in space. The governing equations are box filtered in the LES method, for a one dimensional filter the filter is:

$$\overline{\Phi}(x,t) = \frac{1}{\Delta x}\int_{-0.5\Delta x}^{0.5\Delta x} \Phi()\,dx \tag{2.44}$$

$$\Phi = \overline{\Phi} + \Phi'' \tag{2.45}$$

With this applied to the Navier- Stokes equations, the filtered momentum equations takes the form:

$$\rho\frac{D\overline{u_i}}{Dt} = -\frac{\partial\overline{p}}{\partial x_i} + \mu\frac{\partial}{\partial x_j}\frac{\partial\overline{u_i}}{\partial x_j} - \rho\frac{\partial}{\partial x_j}\left(\overline{u_i u_j} - \overline{u_i}\,\overline{u_j}\right) \tag{2.46}$$

The term $\overline{u_i u_j} - \overline{u_i}\,\overline{u_j}$ are referred to as the subgrid stresses.

This filter is not the same as the Reynolds average in the RANS equations. There are some differences between the filtering in LES and the average in RANS. In the RANS equations the number of times the average function is applied does not matter but in LES it is important to keep in mind that:

$$\overline{\Phi''} \neq 0 \tag{2.47}$$

$$\overline{\overline{\Phi''}} \neq \overline{\Phi''} \tag{2.48}$$

Since a filter is used, a model for the sub grid scales is introduced.

3 Methods, Models and Numerics

This chapter is used to explain how the governing equations are modelled in different models. A brief description of the basics of computational fluid dynamics (CFD) is also given. Some differences between OpenFOAM and CFX are also pointed out.

3.1 Computational Fluid Dynamics Codes

All CFD codes contain the same three basic steps, preprocessing, solving and postprocessing. Preprocessing involves domain definition and setting of boundary conditions and physics. Solving is the process of generating a solution to the set of equations under the given conditions. Postprocessing is the evaluation of the solution given in the previous solver. There are softwares that specialises in just one part of the process and others that do all three steps. OpenFOAM does all three to some extent. OpenFOAM has the ability to create computational domains by a series of definition files. The boundary conditions, physics and other settings are defined in a series of different text files. The solver part of OpenFOAM generates a solution through one of the standard solvers or a solver programmed by the user. The postprocessing can to some extent be done in OpenFOAM. There is a postprocessor, paraView that comes with the installation as a third party software. In both the pre- and post- processing the user can import or export files to other softwares.

3.1.1 Finite volume

To be able to solve the complicated equations in chapter 2, the equations have to be discretised. There are different ways of discretising of which the finite volume method is the most common. In the finite volume discretisation process the computational domain is divided in to several smaller volumes, known as cells. A single cell has to be large enough to encompass a number of molecules so that the smallest fluctuations are averaged out. This is not of concern in most cases since it is well below the kolmogorov length scale. A single cell must also be small enough to assume a constant value of all the properties. The cell size needs to be so small, the mesh can resolve the smallest movements of the flow. How small the cell size needs to be is dependent on the particular case.

3.1.2 Solver types

In the finite volume method the equations are first integrated over all control volumes. Secondly, the equations are discretised with a chosen scheme. The algebraic equations are finally solved with an iterative method.

The discretisation can be done with many different schemes. There are different schemes for different types of terms. The user can also make the choice of accuracy by choosing between different schemes.

3.1.3 Boundary conditions

In order to close the system of equations appropriate boundary conditions has to be given on all boundaries for all variables. The boundary condition can either be prescribed on the value directly or on one of the derivatives.

3.1.4 OpenFOAM, ease of use

OpenFOAM comes without graphical interface, which means that the input data such as boundary conditions, discretisation schemes or solver tolerances are given in a number of input files.

Since OpenFOAM is an open source software it comes without any support. Instead, the user can get help from the Programmer's Guide and User's Guide that is distributed with the program. The OpenFOAM wiki [4], and OpenFOAM forum [3] are also a valuable source of information.

Each OpenFOAM case comes with at least three directories. In the 'system' directory, the definitions regarding the discretisation of all terms and the solver settings for each variable are set. There is also a 'controlDict' file where overarching settings are given, such as maximum number of iterations and routines for saving data.

The 'constant' dictionary is used for modelling and physical properties. Properties for turbulence modelling and the modelling constants that is needed are given here. In the constant dictionary there is also a subdictionary called 'polyMesh' where the computational domain and mesh is specified.

There is also a '0' directory where the boundary and initial conditions are given. All boundary conditions are given for all variables. As for the discretisation schemes there are a variety of boundary conditions to choose from. One of the main advantages of OpenFOAM is that the user is able to create a new boundary condition if the existing ones are not suitable.

3.2 Turbulence Models

There are many models for turbulent flow. In this section only the turbulence models that have been used in the thesis are presented.

3.2.1 $k-\epsilon$

Equation 2.37 is modelled with the equation:

$$\rho\frac{Dk}{Dt}=\frac{\partial}{\partial x_j}\left(\mu+\frac{\mu_t}{\sigma_k}\frac{\partial k}{\partial x_i}\right)-2\mu_t S_{ij}S_{ij}-\rho\epsilon \tag{3.1}$$

The Boussinesq assumption have been used in the production term, $-2\mu_t S_{ij}S_{ij}$, to model the Reynolds stresses.

The dissipation of kinetic energy, ϵ, is modelled with a transport equation of its own. The transport equation is now formulated with the same strategy as the kinetic energy. The same three basic terms of the k equation, production, convection, diffusion and dissipation is present also in the ϵ equation. The production and dissipation are assumed to be proportional to the production and dissipation of kinetic energy. The ϵ equation is written:

$$\rho\frac{D\epsilon}{Dt}=\frac{\partial}{\partial x_j}\left(\mu+\frac{\mu_t}{\sigma_\epsilon}\frac{\partial \epsilon}{\partial x_i}\right)-C_{1\epsilon}\frac{\epsilon}{k}2\mu_t S_{ij}S_{ij}-C_{2\epsilon}\rho\frac{\epsilon^2}{k} \tag{3.2}$$

Both the production and dissipation term have been multiplied with $\frac{\epsilon}{k}$ to get the correct dimension, kinetic energy per time $\left[\frac{L^2}{T^3}\right]$

The constants for the standard $k-\epsilon$ are [7]:

$$C_\mu = 0.09 \tag{3.3}$$

$$\sigma_k = 1 \tag{3.4}$$

$$\sigma_\epsilon = 1.3 \tag{3.5}$$

$$C_{1\epsilon} = 1.44 \tag{3.6}$$

$$C_{2\epsilon} = 1.92 \tag{3.7}$$

3.2.2 $k-\omega$

Instead of using the length scale $\ell = k^{3/2}/\epsilon$ as for the $k-\epsilon$ model, it has been proposed to use $\ell = k^{1/2}/\omega$ as the turbulence length scale where ω is the turbulence eddy frequency. Using this relation, the kinetic energy equation is written:

$$\rho\frac{Dk}{Dt} = \frac{\partial}{\partial x_j}\left(\mu + \frac{\mu_t}{\sigma_k}\frac{\partial k}{\partial x_i}\right) - 2\mu S_{ij}S_{ij} - \frac{2}{3}\rho k\frac{\partial U_i}{\partial x_j}\delta_{ij} - \beta^*\rho k\omega \tag{3.8}$$

As for the $k-\epsilon$ model, a transport equation is formulated for the turbulence eddy frequency, ω. This is modelled as:

$$\rho\frac{D\omega}{Dt} = \frac{\partial}{\partial x_j}\left(\mu + \frac{\mu_t}{\sigma_\omega}\frac{\partial \omega}{\partial x_i}\right) + \gamma_1\left(2\rho S_{ij}S_{ij} - \frac{2}{3}\rho\omega\frac{\partial U_i}{\partial x_j}\delta_{ij}\right) - \beta_1\rho\omega^2 \tag{3.9}$$

For the $k-\omega$ equation, the constants are [6]:

$$\sigma_k = 2 \tag{3.10}$$

$$\sigma_\omega = 2 \tag{3.11}$$

$$\gamma_1 = 0.553 \tag{3.12}$$

$$\beta^* = 0.09 \tag{3.13}$$

$$\beta_1 = 0.075 \tag{3.14}$$

3.2.3 Shear stress transport

The shear stress transport (SST) is a model where the $k-\epsilon$ model is used far from walls and the $k-\omega$ model is used for near wall regions. The model is designed to use the advantages from both models. The k equation is the same as the k equation in the $k-\omega$ model, equation 3.8. The ω equation is on the other hand modified. In the SST model the substitution $\epsilon = k\omega$ is made. This leads to the ω equation:

$$\rho\frac{D\omega}{Dt} = \frac{\partial}{\partial x_j}\left(\mu + \frac{\mu_t}{\sigma_{\omega,1}}\frac{\partial \omega}{\partial x_i}\right) + \gamma_2\left(2\rho S_{ij}S_{ij} - \frac{2}{3}\rho\omega\frac{\partial U_i}{\partial x_j}\delta_{ij}\right) - \beta_2\rho\omega^2 + 2\frac{\rho}{\sigma_{\omega,2}\omega}\frac{\partial k}{\partial x_k}\frac{\partial \omega}{\partial x_k} \tag{3.15}$$

The switch between the $k-\epsilon$ and the $k-\omega$ model is done with blending functions. These are applied to constants and the cross- diffusion term, $2\frac{\rho}{\sigma_{\omega,2}\omega}\frac{\partial k}{\partial x_k}\frac{\partial \omega}{\partial x_k}$. A blending function between two constants C_1 in the original $k-\omega$ model and C_2 in the $k-\epsilon$ model is written

$$C = F_C C_1 + (1 - F_C)C_2 \tag{3.16}$$

A blending function tends to zero at the wall and unity far from the wall. Typically, F_C takes the form $F_C = F_C(\ell_t/y, Re_y)$. Where the length scale is $\ell = \sqrt{k}/\omega$, the Reynolds number is $Re_y = y^2\omega/\nu$ and y is the distance from the wall.

To complete the model there also needs to be a set of functions to limit some properties. The turbulent eddy viscosity is limited by

$$\nu_t = \frac{a_1 k}{max(a_1\omega, SF_2)} \tag{3.17}$$

where $S = \sqrt{2S_{ij}S_{ij}}$, a_1 is a constant and F_2 is a blending function.

The production of turbulent kinetic energy is limited by

$$P_k = min\left(10\beta^* \rho k\omega, 2\mu_t S_{ij}S_{ij} - \frac{2}{3}\rho k \frac{\partial U_i}{\partial x_j}\delta_{ij}\right) \tag{3.18}$$

The constants in equation 3.15, are [6]:

$$\sigma_{\omega,1} = 2 \tag{3.19}$$

$$\sigma_{\omega,2} = 1.17 \tag{3.20}$$

$$\gamma_2 = 0.44 \tag{3.21}$$

$$\beta_2 = 0.083 \tag{3.22}$$

3.2.4 Reynolds stress model

In the Reynolds stress method six equations for the Reynolds stresses are solved with the momentum and continuity equation. The Reynolds stress equations can be found in equation 2.40. The model for these equations are given below.

$$\begin{aligned}
\frac{D\overline{u_i u_j}}{Dt} = & \\
& - \overline{u_i u_k}\frac{\partial \overline{U_j}}{x_k} - \overline{u_k u_j}\frac{\partial \overline{U_i}}{x_k} \\
& - c_1 \frac{\epsilon}{k}\left(\overline{u_i u_j} - \frac{2}{3}\delta_{ij} k\right) \\
& - c_2 \left(P_{ij} - \frac{2}{3}\delta_{ij} P^k\right) \\
& + c_1' \rho \frac{\epsilon}{k}\left(\overline{u_k u_m} n_k n_m \delta_{ij} - \frac{3}{2}\overline{u_i u_k} n_k n_j - \frac{3}{2}\overline{u_j u_k} n_k n_i\right)\left(\frac{\ell_t}{x_n}\right) f \\
& + c_2' \left(\Phi_{km,2} n_k n_m \delta_{ij} - \frac{3}{2}\Phi_{ik,2} n_k n_j - \frac{3}{2}\Phi_{jk,2} n_k n_i\right)\left(\frac{\ell_t}{x_n}\right) f \\
& + \nu \frac{\partial^2 \overline{u_i u_j}}{\partial x_k \partial x_k} \\
& + \frac{\partial}{\partial x_k}\left[\left(\nu + c_k \overline{u_k u_m}\frac{k}{\epsilon}\right)\frac{\partial^2 \overline{u_i u_j}}{\partial x_m}\right] \\
& - \frac{2}{3}\epsilon\delta_{ij}
\end{aligned} \tag{3.23}$$

In the equations above, P_{ij} and P^k are production of Reynolds stress and kinetic energy. The kinetic energy is found by taking the trace of the Reynolds stresses, i.e. $P^k = \frac{1}{2}P_{ll}$. P_{ij} is a term in the equation, namely

$$P_{ij} = \overline{u_i u_k}\frac{\partial \overline{U_j}}{\partial x_k} - \overline{u_k u_j}\frac{\partial \overline{U_i}}{\partial x_k} \tag{3.24}$$

n is the distance to the wall and is found in the wall damping functions. Φ comes from the modelled pressure strain term and reads

$$\Phi_{ij,1} = -c_1 \frac{\epsilon}{k}\left(\overline{u_i u_j} - \frac{2}{3}\delta_{ij} k\right) \tag{3.25}$$

$$\Phi_{ij,2} = -c_2 \left(P_{ij} - \frac{2}{3}\delta_{ij} P^k\right) \tag{3.26}$$

f makes sure that the terms that are multiplied with f are only valid near the wall through

$$f = \frac{k^{3/2}}{2.55 x_n \epsilon} \tag{3.27}$$

Together with the six Reynolds stress equations, a turbulence eddy dissipation is solved. In CFX, the turbulence eddy dissipation equation is formulated as equation 3.28. This is a simplified version of the turbulence eddy dissipation equation, similar to those of the $k-\epsilon$ and $k-\omega$ models.

$$\rho \frac{D\epsilon}{Dt} = \frac{\partial}{\partial x_j}\left(\mu + \frac{\mu_t}{\sigma_\epsilon}\frac{\partial \epsilon}{\partial x_i}\right) - C_{1\epsilon}\frac{\epsilon}{k}P^k - C_{2\epsilon}\rho\frac{\epsilon^2}{k} \tag{3.28}$$

3.2.5 Large eddy simulations

LES, large eddy simulations, uses a model for the flow at subgrid scales, see section 2.2.2. One such model is the Smagorinsky model where the sub grid stresses are modelled as:

$$\overline{u_i u_j} - \overline{u_i}\,\overline{u_j} = -2\nu_{SGS}\overline{s}_{ij} \tag{3.29}$$

$$\nu_{SGS} = (C_s \Delta)^2 \sqrt{2\overline{s}_{ij}\overline{s}_{ij}} \tag{3.30}$$

$$\overline{s}_{ij} = \frac{1}{2}\left(\frac{\overline{u}_i}{x_j} + \frac{\overline{u}_j}{x_i}\right) \tag{3.31}$$

$$\Delta = (\delta V)^{1/3} \tag{3.32}$$

The local cell size Δ is a part of the model which means that there is a grid dependence in the model. If the cut off filter size is taken in the inertial subrange, the kinetic energy is decaying as $\kappa^{-5/3}$. The Smagorinsky constant can be calculated to be C_s is 0.17 [1]. However other values of the Smagorinsky constant are used depending on the mesh resolution and case.

3.2.6 Scalar transport

The scalar transport equation found in section 2.1.4, is modelled with the equation

$$\rho \frac{Dc}{Dt} = \left(\frac{\nu}{Sc} + \frac{\nu_t}{Sc_t}\right)\frac{\partial^2 c}{\partial x_j^2} \tag{3.33}$$

where the viscosity, ν, is material dependent. The turbulent viscosity ν_t is acquired from the turbulence model. The Schmidt number, Sc, is a constant that is set to 0.9 in CFX.

4 Measurements

Measurements were made in the water rig by Siemens and the data were post processed at Siemens.

4.1 Siemens Water Rig

To be able to study the flow in the burner more in detail, Siemens has constructed a water rig. The rig uses water as a medium to study the flow in the burner. Both the air and the gas flows in the burner are studied with water. To differentiate between the two different flows, gas and air, there is a tracer in the water that is used in the gas inflow. The tracer is premixed with some of the water. The setup of the water rig is schematically shown in figure 4.1.

4.2 Measurement Method

In the rig, Siemens is able to study different burners and burner alterations. The amount of inflow of water has been studied in previous work and has been found to be 4 kg/s of water through the air inlets and 0.11 kg/s of water through the gas inlets [2].

The only measurement that is being made in the water rig is the tracer distribution. The tracer distribution is measured up- stream of the combustion chamber. To measure the tracer distribution a laser is used to enlighten the water. The tracer then lights up in this laser cross section only. To be able to fit the laser sheet in the burner, the burner has been slightly extended with a Plexiglas section. A camera is mounted on top of the water rig, pointing down the burner towards the laser cross section. The camera takes several pictures at the tracer distribution.

4.3 Data Reduction

The pictures of the tracer distribution are post processed in a computer where the pixel intensity is measured in the pictures. Since the tracer concentration varies between different mixings, the pixel intensity is normalised by the sum of pixel intensities, thus ensuring that a series of measurements can be compared with other measurements. In a series of pictures, the mean and RMS value of the pixel intensity distribution is found, which is assumed to be proportional to the tracer distribution.

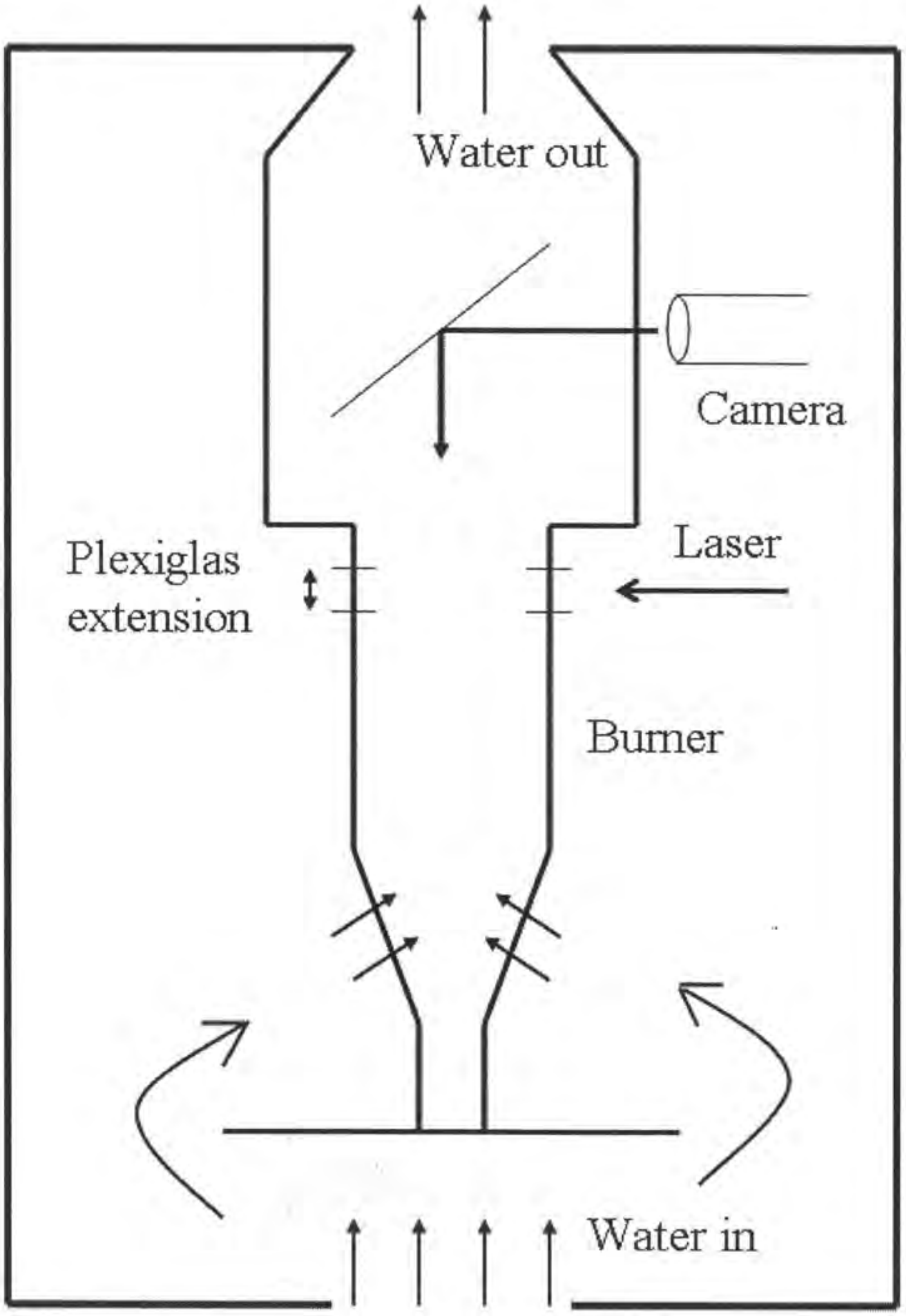

Figure 4.1: Schematic figure of the water rig.

5 Simulation

This chapter aims to present the simulations so that anyone with knowledge of the geometry can reproduce the results. If the geometry is not known the given simulation description should be enough to understand the simulation setup. Part of the burner geometry is visible in figure 5.1.

5.1 Mesh

A computational mesh is used to describe the geometry with small elements. The domain is discretised so that the equations can be solved for each cell. It is important to keep in mind that some numerical models, e.g. the Smagorinsky LES model, are dependent on a good mesh. A good mesh is a mesh where the growth rate or volume ratio between neighbouring cells are small and the cells have a nice shape. The cell quality in terms of cell shape can be measured by how close they resemble the ideal shape. There are guidelines about how far from ideal cell shape the elements should be. For prisms and hexahedral cells, the aspect ratio or length ratios between the different cell lengths must not be to large.

Figure 5.1: Part of the geometry.

The skewness quality is calculated with the equilateral volume deviation method in the commercial software TGrid. The method is defined as

$$Skewness = \frac{OptimalCellSize - CellSize}{OptimalCellSize} \tag{5.1}$$

The optimal cell size is calculated by calculating the size of an equilateral cell with the same circumradius. A low value on 'Quality' in figures 5.3- 5.5 indicates a good mesh.

5.1.1 Mesh with tetrahedrons

At the start of the project a mesh with only tetrahedrons was provided by Siemens Industrial Turbomachinery. The mesh had been used earlier in both RANS and LES simulations under operating conditions. The cell quality of the mesh can be seen in figure 5.3. The mesh will from here on be referred to as the 'tet mesh'.

5.1.2 A mixed mesh

A mesh was generated by the author early in the project using the commercial software ANSA. The aim of the mesh generation was to have as large part of the volume as possible discretised with hexahedral cells. First, the easier parts were meshed with hexahedrons and then tetrahedrons were used for the parts with more difficult geometry. Another aim was also to create a mesh where the regions with high gradients had a hexahedral mesh. The mesh quality can be seen in figure 5.4. The mesh will from here on be referred to as the 'mix mesh 1'.

5.1.3 Another mixed mesh

A refined mesh was also generated with the same aim as the previous mixed mesh, i.e. to use many hexahedral cells and resolve areas with high gradients with hexahedrons. Lessons learnt from the previous mesh were used to create a better second mesh. Parts of the volume that had bad elements in the first mesh were now being resolved with an alternate strategy. Some more cells were also added to the mesh. A part of the mesh can be seen in figure 5.2. The cell quality can also be seen in figure 5.5. The mesh will from here on be referred to as the 'mix mesh 2'.

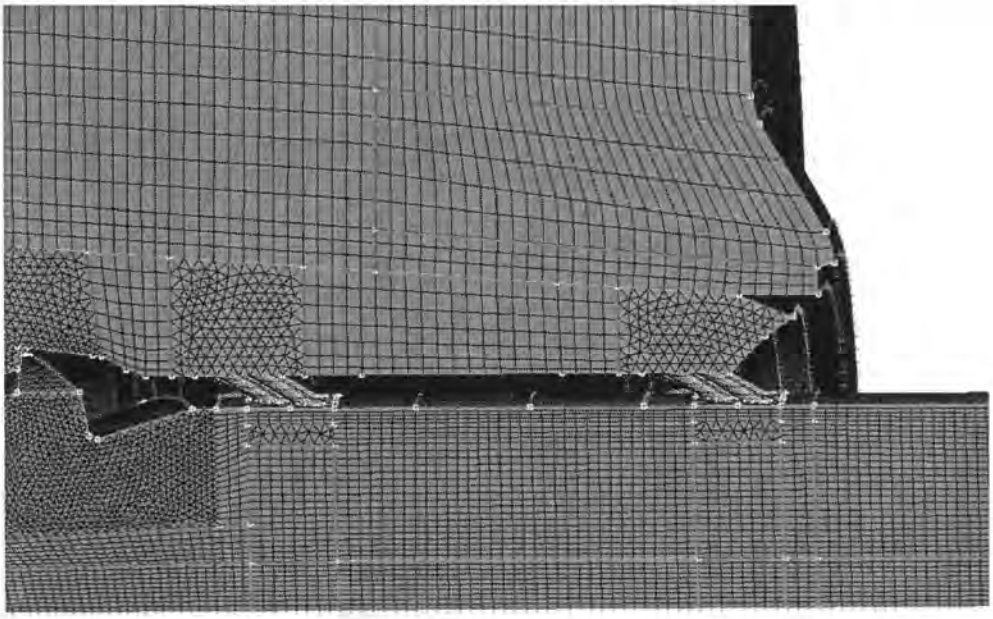

Figure 5.2: Part of mix mesh 2.

5.2 Setup and Boundary Conditions

It is important to set boundary conditions at all boundaries, surrounding the computational domain. Boundary conditions for all parameters that is solved for have to be set. It is also possible to choose in which way to discretise the equations.

The turbulence model that has most commonly been used is the $k-\omega$ SST model. The $k-\epsilon$ model and the Reynolds stress models have also been used, but only in CFX.

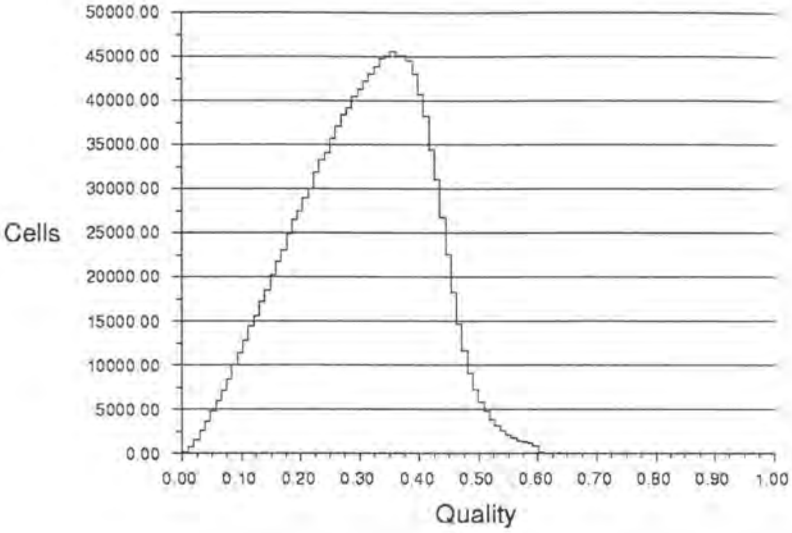

Histogram of Cell Quality, Equilateral Volume Deviation Method

May 23, 2009
TGrid 5.0 (3D)

Figure 5.3: Cell quality of tet mesh.

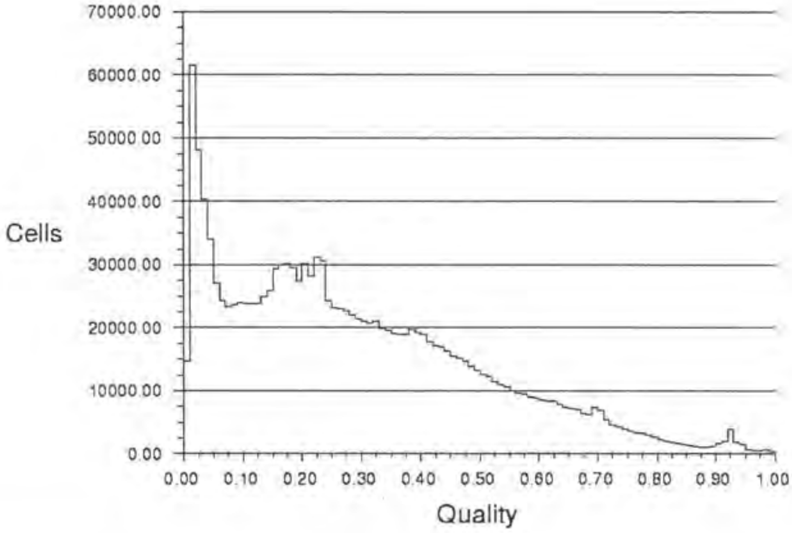

Histogram of Cell Quality, Equilateral Volume Deviation Method

May 23, 2009
TGrid 5.0 (3D)

Figure 5.4: Cell quality of mix mesh 1.

	Number of elements	Tetrahedrons volume %	Hexahedrons volume %	Maximal skewness
tet mesh	1.3 M	100	0	0.92
mix mesh 1	1.5 M	2.5	97.5	1
mix mesh 2	2.2 M	2.3	97.7	0.93

Table 5.1: Number of elements, cell type and quality distribution for different meshes.

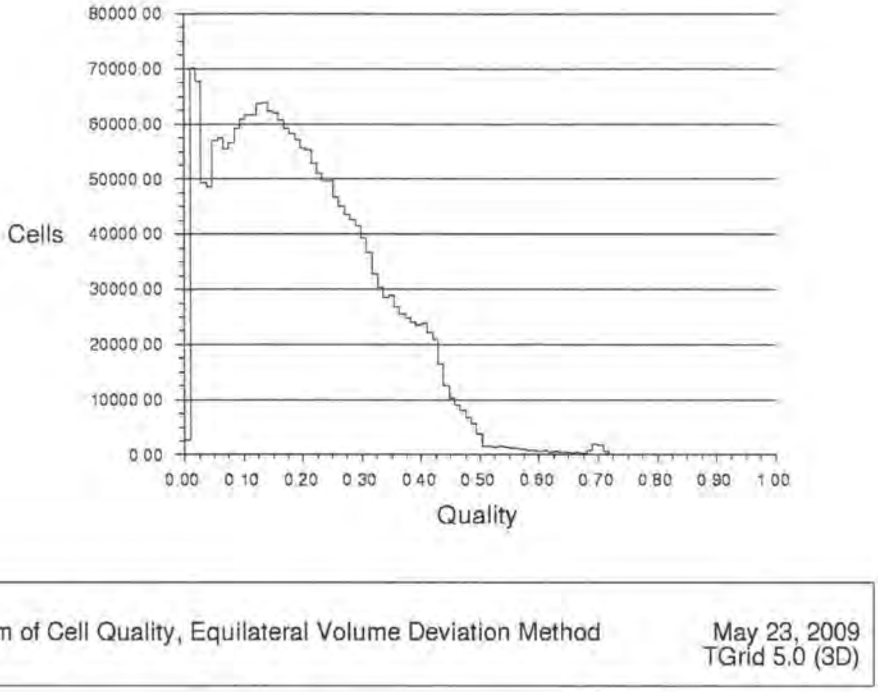

Figure 5.5: Cell quality of mix mesh 2.

5.2.1 Boundary conditions

The way in which the boundary conditions are set in OpenFOAM and CFX are a bit different. In CFX most of the boundary conditions are set automatically. In OpenFOAM all the boundary conditions have to be set explicitly, including the turbulent quantities.

The walls in the burner were all treated as no-slip walls where the velocity is zero and the pressure and scalar equations use a zero gradient boundary condition. For the turbulence quantities, the wall boundary condition is less straight forward. As the velocity goes to zero at the wall, so does the kinetic energy. For the turbulence eddy dissipation, ϵ, it is assumed that the dissipation of kinetic energy is proportional to the kinetic energy and it also goes to zero at the wall. One of the advantages of the $k-\omega$ SST model is that it switches to a $k-\omega$ model near walls, but ω goes to infinity as the wall distance goes to zero. These boundary conditions only apply when the grid is fine enough to keep the dimensionless length to the first cell, y^+, less then 5. When the dimensionless length is greater a wall function is used where the first cell in the domain is given a non-zero value.

The velocity at the inlets were set according to the experiment velocities that were specified by Siemens. In CFX the turbulence intensity was also set to be 5 %, this turbulence intensity was used to estimate the turbulence kinetic energy at the inlets that were used in OpenFOAM. In the same way, the turbulence eddy frequency, ω, has to be estimated in order to prescribe the correct inlet conditions in OpenFOAM. For this estimation the turbulence eddy length was assumed to be approximately 20 % of the inlet diameter. With this knowledge a turbulence dissipation could be estimated and the turbulence frequency could then be found as the dissipation divided by the kinetic energy. The scalar was also prescribed at the inlets, with the value 0 for inlets where air normally flows and 1 for inlets where gas normally flows.

For the calculations, the following equations were used to estimate k and ω:

$$k = \frac{3}{2}(UI)^2 \tag{5.2}$$

$$\omega = \frac{C_\mu^{0.75} k^{\frac{3}{2}}}{\ell} \frac{1}{k} \tag{5.3}$$

where I is the turbulence intensity and ℓ is a turbulence length scale, which is the diameter times a length ratio.

At the outlet, the pressure outlet boundary condition is used. This includes setting the pressure to 0 and using zero gradient for all other quantities.

5.2.2 Discretisation

Again, CFX and OpenFOAM differs quite a lot on this point. In CFX the choice is made in the case setup between an upwind or a high resolution scheme. In OpenFOAM however, the same type of term in all equations can be set as a default scheme. Each term in every equation can also be given an unique scheme.

For the CFX simulations the high resolution scheme was used for the velocity and continuity equations but the less accurate upwind scheme was used for the turbulent quantities. The schemes in OpenFOAM that were used for the discretisation were in most cases upwind for the divergence terms and central scheme for the laplacian terms.

5.3 Convergence

Since the discretised equations are solved with an iterative process a measurement of the solution is needed. The convergence is a measure of how close the present solution is to a steady solution. A steady solution is a solution were any additional iterations do not change the solution.

For cell P an equation is formulated for the value of any variable Φ.

$$(a_P \Phi_P)_i = \left(\sum_{nb} a_{nb} \Phi_{nb} \right)_i + b_i \tag{5.4}$$

After solving for all cells, the difference between the right hand and the left hand side of equation 5.4 is called the local residual. The sum of all absolute values of all local residuals is the global residual. If the solution converges the value of the global residual decrease. The problem with residuals are that a small decrease of many local residuals can cancel out a large increase of a few local residuals and it is also difficult to decide what value of the global residual is low enough for a specific case.

Because of this difficulty, monitors were used in the burner simulations to verify convergence.

6 Test case

A simple test case was created to investigate the characteristics of OpenFOAM. The main aim of the test case is to investigate what differences there are in mass transport between CFX and OpenFOAM. The test case was included in the thesis after some unsatisfactory results of the scalar transport had been seen in OpenFOAM.

6.1 Geometry and Mesh

The simple geometry is a flow between two circular pipes, see figure 6.1. The inlet was split in half to allow for a scalar to be added at one of the halves. One surface quadrilateral mesh was used for all cases but three different volume meshes were generated. The three different meshes were a hexahedral mesh, a coarser tetrahedral mesh and a finer tetrahedral mesh. The resulting mesh sizes are approximately 42 000 cells for the hexahedral mesh, 195 000 cells for the coarser tetrahedral mesh and 603 000 cells for the finer tetrahedral mesh. The difference in mesh generation between the tetrahedral meshes is the allowed growth rate in the volume mesh generation, 1.2 for the coarser mesh and 1.05 for the finer mesh.

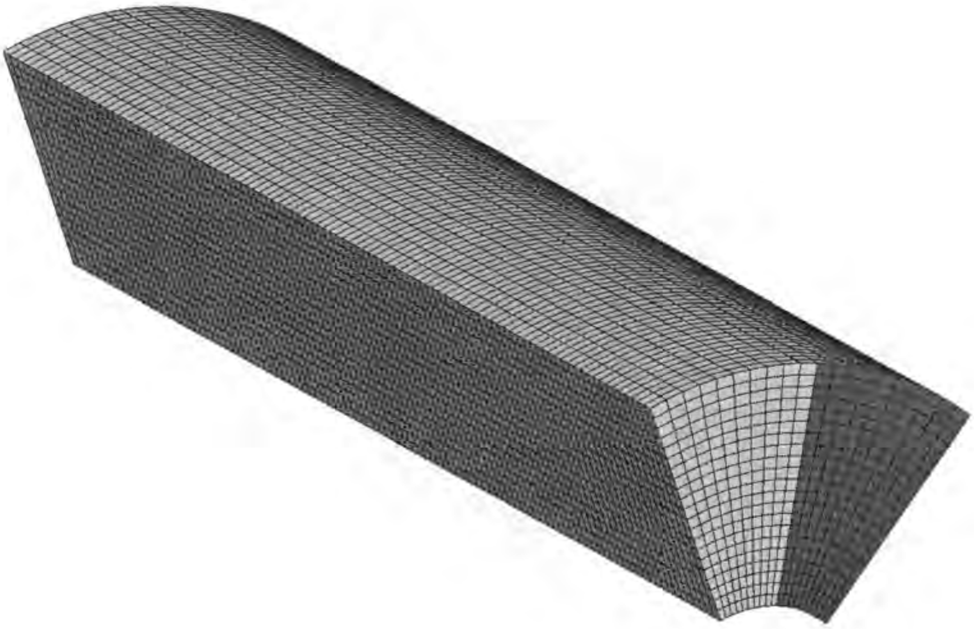

Figure 6.1: Geometry and surface mesh of test case with the split inlet visible.

The dimensions of the geometry are inner radius, 1 cm, outer radius, 3 cm, and length, 10 cm. The angle between the periodic sides are 60°.

6.2 Boundary Conditions and Setup

The same way as in the real case of prescribing boundary conditions and setups were used in the test case, see 5.2 for a closer description.

The medium used in the calculations are water with the kinematic viscosity, $\nu = \mu/\rho = 10^{-6}$. A scalar was added to one of the inlets in OpenFOAM and in CFX, the water from the different inlets could be tracked. The velocity at both of the inlets was set at 1 m/s in the direction of the pipe which makes for the Reynolds number

$$Re_d = \frac{Ud}{\nu} = \frac{1 \cdot 0.02}{10^{-6}} = 20000 \tag{6.1}$$

For the inlets the turbulence quantities k and ω were estimated to be

$$k = \frac{3}{2}(UI)^2 = \frac{3}{2}(1 \cdot 0.05)^2 = 0.00375 \tag{6.2}$$

$$\omega = \frac{C_\mu^{0.75} k^{\frac{3}{2}}}{\ell} \frac{1}{k} = \frac{0.09^{0.75} 0.00375^{\frac{3}{2}}}{0.075 \cdot 0.2} \frac{1}{0.00375} = 0.67 \tag{6.3}$$

where the length scale ℓ is calculated as the square root of the area times the turbulence eddy length ratio, 0.2.

6.3 Results

The evaluation of the results are aimed at the mixing of the water flowing in through the two inlets. There are three questions that are asked in the following sections, how should the diffusive term in the scalar transport equation be modelled, what is the influence of mesh resolution and finally how does the results differ between CFX and OpenFOAM. The mixing between the two inlets at an isosurface can be seen in figure 6.2.

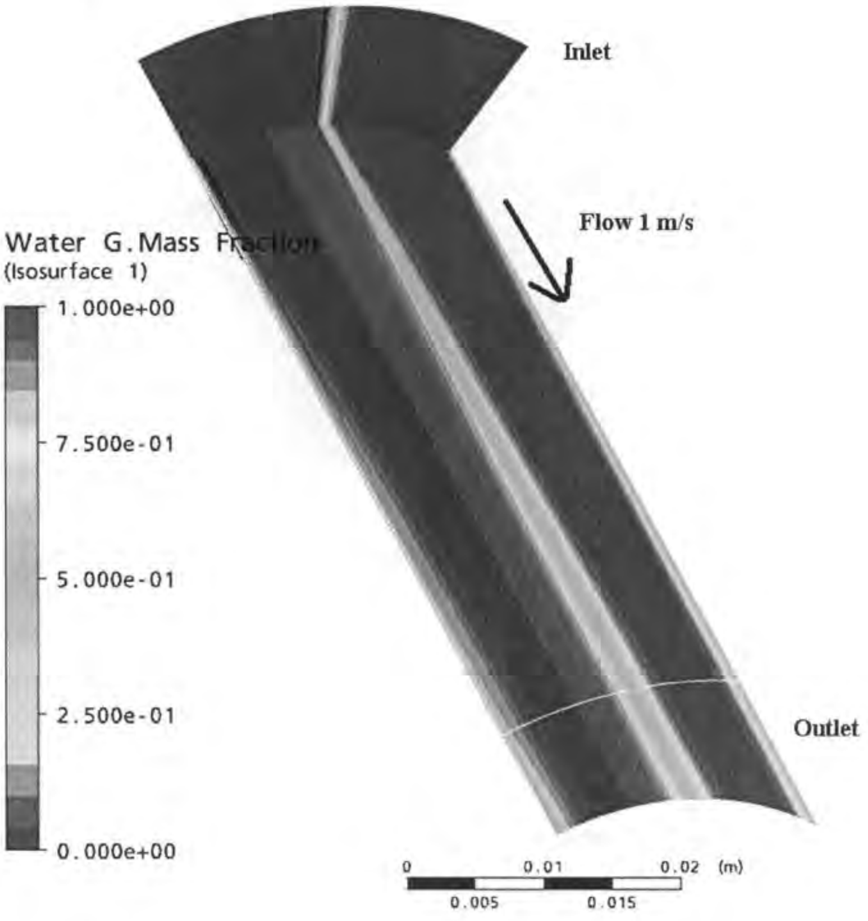

Figure 6.2: Scalar concentration at an isosurface in the middle of the domain.

In all cases the scalar distribution are evaluated at the outlet, at a line at equal distance from the two walls.

6.3.1 Scalar transport diffusive term

The diffusive term in the modelled scalar transport equation is written

$$\frac{\partial}{\partial x_j}\left(\nu + \frac{\nu_t}{Sc}\right)\frac{\partial c}{\partial x_j} \tag{6.4}$$

where c is the scalar concentration and Sc is the turbulent Schmidt number. In figure 6.3 the results can be seen from simulations with different Schmidt numbers. The simulations were done with the hexahedral mesh. In CFX, the default value for the turbulent Schmidt number is 0.9. Considering the Schmidt number in CFX, the range of Schmidt numbers in the OpenFOAM simulations is very large. This means that only a rough estimation of the Schmidt number can be given. The Schmidt number range in figure 6.3 is in orders of magnitude and the Schmidt number should preferably be set with more accuracy.

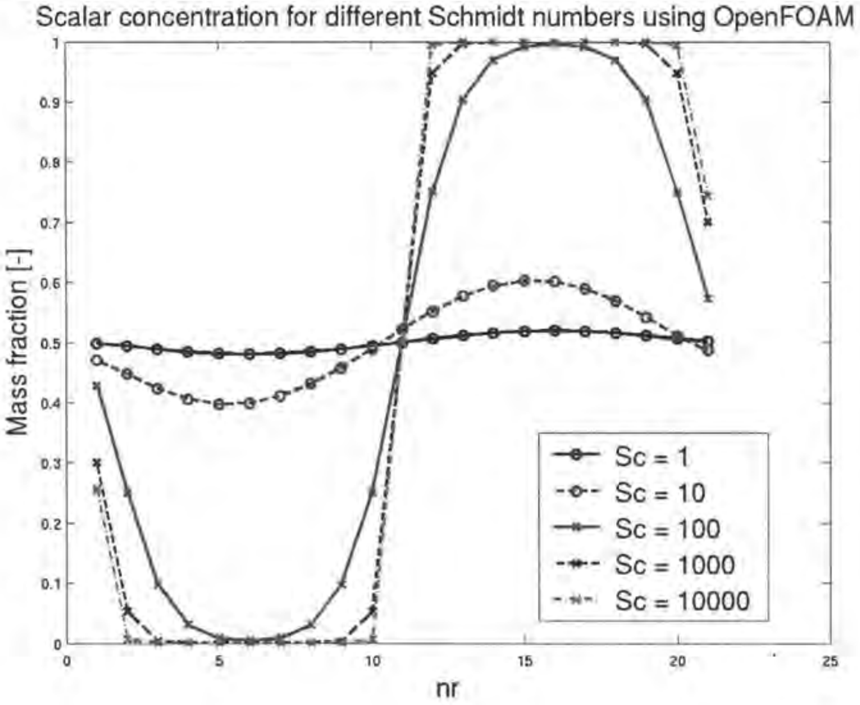

Figure 6.3: Scalar concentration for different Schmidt numbers using OpenFOAM.

6.3.2 Mesh dependence

The difference between tetrahedral meshes was also investigated for both CFX and OpenFOAM. In figure 6.4, the results from CFX can be seen. It is evident in figure 6.6 that the scheme resolution is important for the cases with tetrahedral meshes. For the case with high resolution schemes on the tetrahedral mesh, the difference between the scheme resolution is substantial.

6.3.3 Differences between CFX and OpenFOAM

The results from the different codes have been presented together, in figure 6.5 for the hexahedral mesh and in figure 6.6 for the finer tetrahedral mesh. In figure 6.5 the results from two different Schmidt numbers in OpenFOAM have been included. The difference is larger between OpenFOAM and CFX when using a tetrahedral mesh. However, the

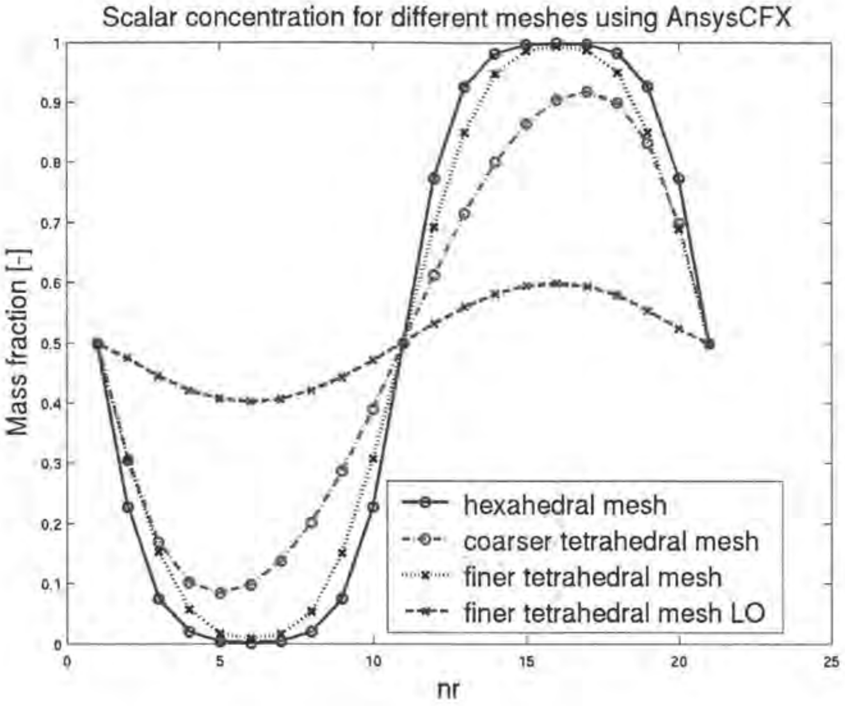

Figure 6.4: Scalar concentration for different meshes using CFX.

OpenFOAM solution shows that the first order upwind scheme is better in OpenFOAM than in CFX.

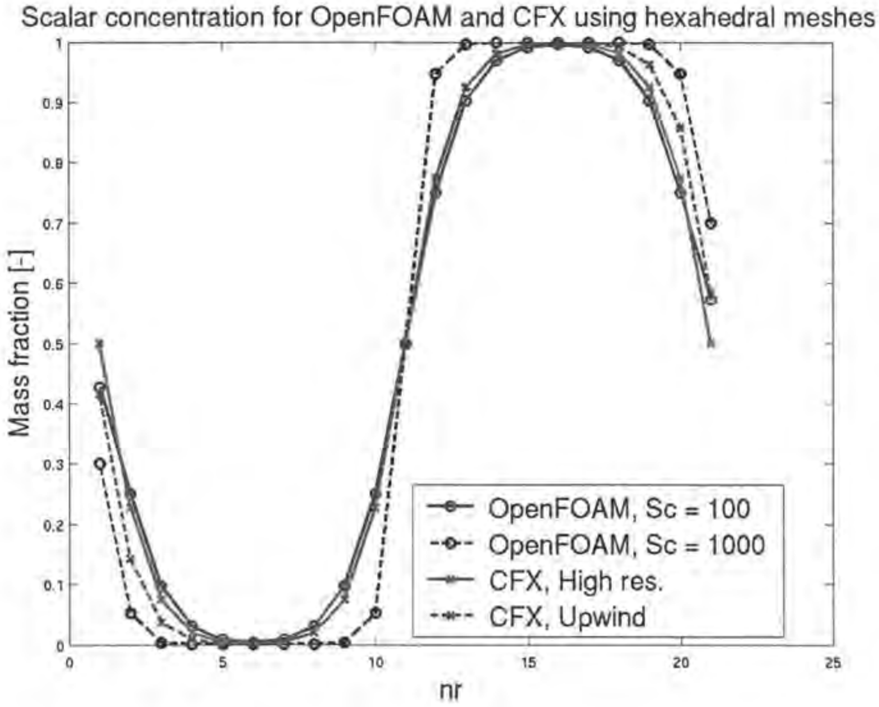

Figure 6.5: Scalar concentration for OpenFOAM and CFX using hexahedral meshes.

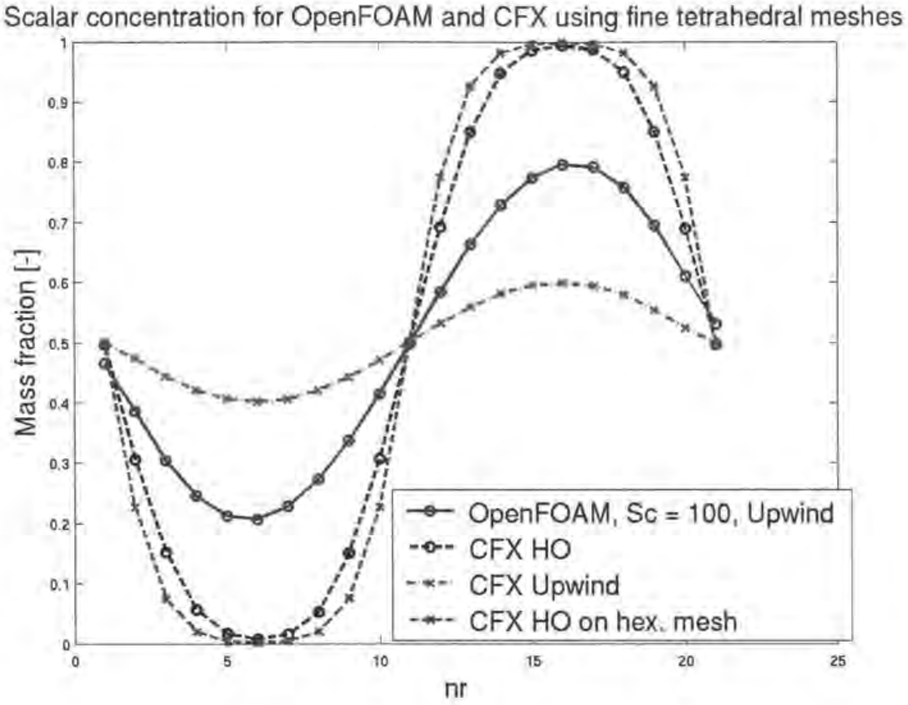

Figure 6.6: Scalar concentration for OpenFOAM and CFX using a fine tetrahedral mesh.

6.3.4 Convergence rate

The convergence rate for the test case has been plotted. The results show the convergence rate for OpenFOAM, figure 6.7 and for CFX, figure 6.8. It can be seen that CFX has a much faster convergence rate than OpenFOAM. However, it should be noted that nothing were done in this case to minimize the number of iterations. OpenFOAM might very well be in line with CFX for convergence rate when better solver settings are used.

6.3.5 Conclusions

Out of the Schmidt numbers tested in OpenFOAM, the Schmidt number that is most suitable in OpenFOAM is 100. This Schmidt number is only an estimate. There is no more in this report, than a CFX simulation to support the choice of this Schmidt number. It has not been investigated how good the Schmidt number in CFX is, only the default value, 0.9, has been used.

After reviewing the results above it is clear that there is a strong mesh dependence in both CFX and OpenFOAM. It can also be seen that the scheme resolution is more important when using tetrahedral meshes than in the cases where a hexahedral mesh have been used.

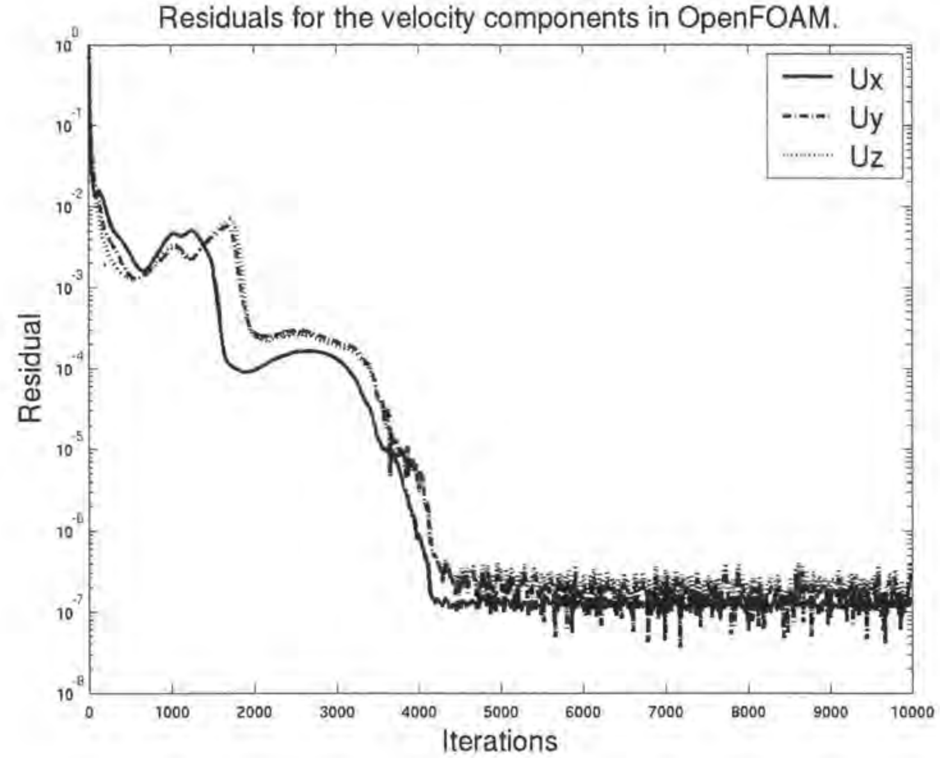

Figure 6.7: Residuals for the velocity components in OpenFOAM.

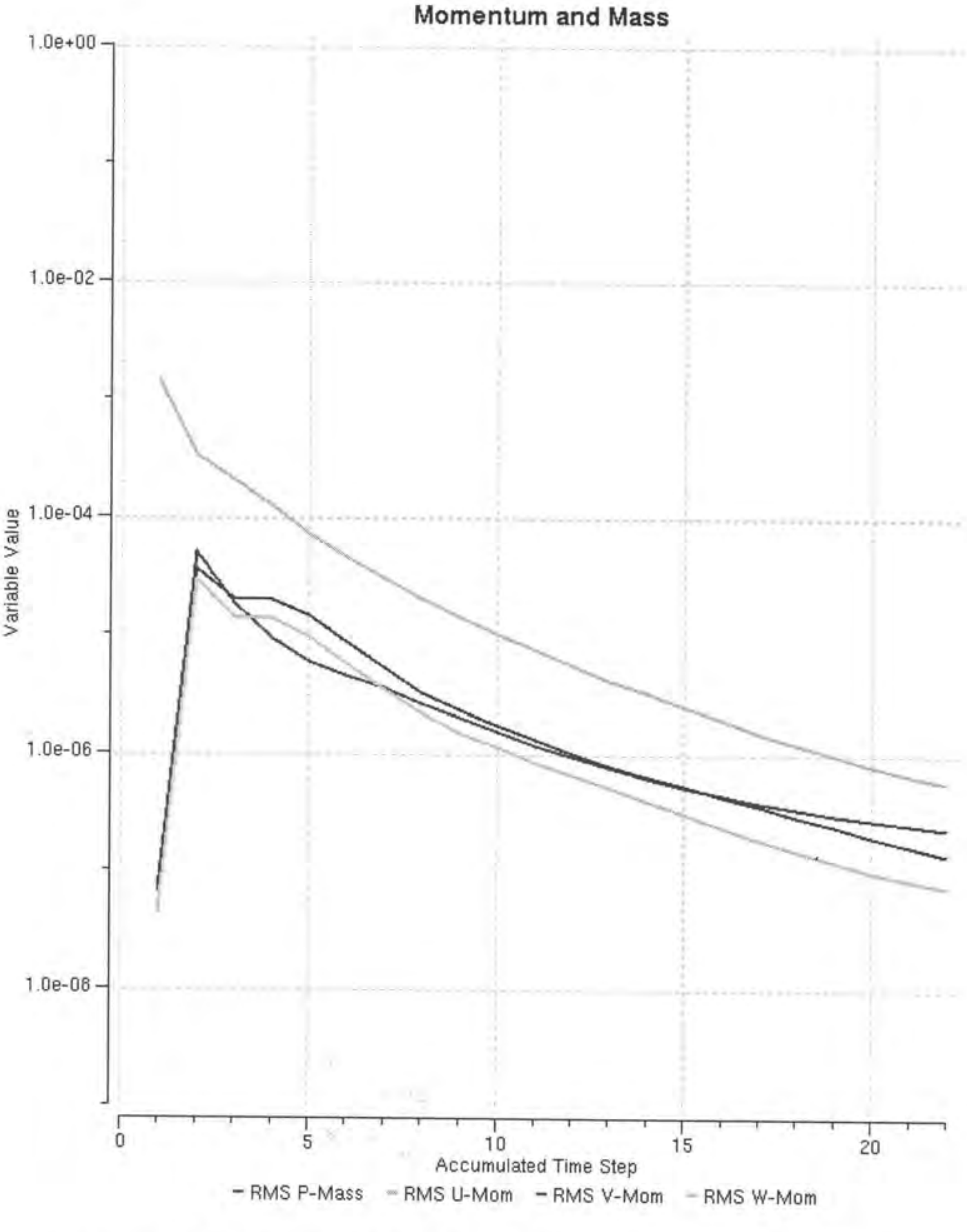

Figure 6.8: Residuals for the velocity components in CFX.

7 Results

The results from the simulations are evaluated at the centre line and at three planes in the mixing tube. The plane at $\frac{x}{D} = -0.8$, upstream from the mixing tube outlet is the same as the laser sheet plane. The three planes are marked out in figure 7.1. The evaluation along centre line at radius r = 0 has been made in the entire domain where $x = 0$ is at the mixing tube outlet into the combustion chamber.

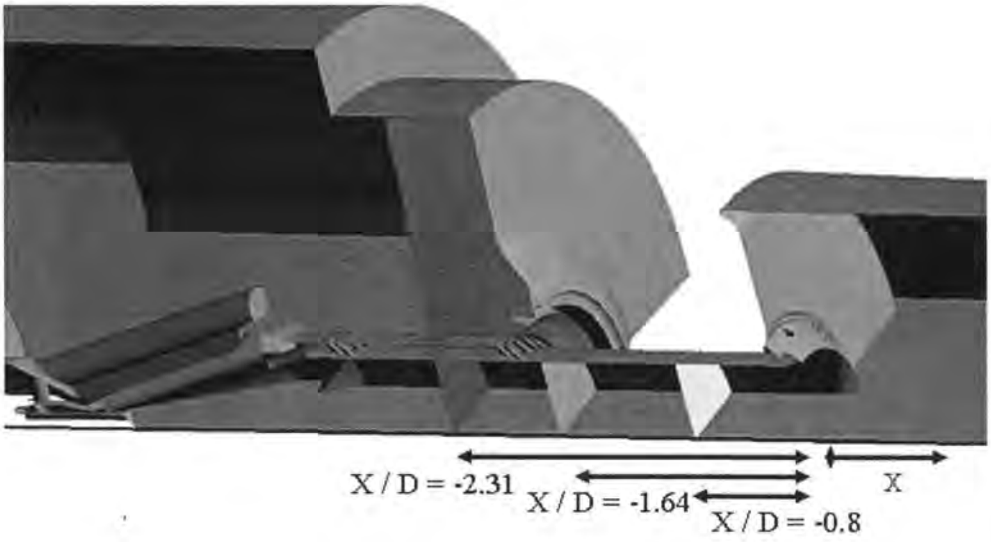

Figure 7.1: Three planes for result evaluation.

In this chapter some of the more important results are presented. For more results, please see Appendix B.

7.1 Swirl Number

The swirl number is defined as

$$Sw = \frac{\int_0^R u_x u_t r^2 \, dr}{R \int_0^R u_x^2 r \, dr} \tag{7.1}$$

In words this can be described as the angular momentum divided by the axial momentum. The swirl in a pipe should decrease since there is nothing to create swirl and the flow should go towards axial flow. After the first evaluation plane at $\frac{x}{D} = -2.31$ there are a set of film holes where more air is injected. These film holes are tilted to create swirl. It is unknown if the added swirl in these film holes are more than the decreasing swirl in the section between the first and second evaluation plane.

In tables 7.1, 7.2 and 7.3 the swirl number is presented for different simulations. There is a decrease in swirl number in the simulations with both OpenFOAM and CFX. There is however a substantial difference between the magnitudes of the swirl numbers for OpenFOAM and CFX. OpenFOAM shows a lower angular momentum than CFX in section B.1 but again they follow the same pattern in the different evaluation planes where there is an increase between evaluation plane one and two and a decrease between two and three.

It is also evident from section B.1 that all RANS simulations follow the same pattern in swirl number numerator value. There is an increase between evaluation plane one and two followed by a decrease between evaluation plane two and three. However, the incomplete

LES simulation shows no increase between evaluation plane one and two but a decrease all the way through the three evaluation planes.

	OpenFOAM			CFX		
	tet mesh	mix mesh 1	mix mesh2	tet mesh	mix mesh 1	mix mesh2
SST First order scheme	-	-	0.569	-	-	0.465
SST High order scheme	-	-	-	0.472	0.5	0.494
k- ϵ	-	-	-	0.497	-	0.54
RSM	-	-	-	-	-	0.479
LES	-	-	-	-	-	0.507

Table 7.1: Swirl number at $\frac{x}{D} = -2.31$ from the combustion chamber opening.

	OpenFOAM			CFX		
	tet mesh	mix mesh 1	mix mesh2	tet mesh	mix mesh 1	mix mesh2
SST First order scheme	-	-	0.514	-	-	0.43
SST High order scheme	-	-	-	0.456	0.496	0.501
k- ϵ	-	-	-	0.49	-	0.521
RSM	-	-	-	-	-	0.441
LES	-	-	-	-	-	0.455

Table 7.2: Swirl number at $\frac{x}{D} = -1.64$ from the combustion chamber opening.

	OpenFOAM			CFX		
	tet mesh	mix mesh 1	mix mesh2	tet mesh	mix mesh 1	mix mesh2
SST First order scheme	-	-	0.465	-	-	0.407
SST High order scheme	-	-	-	0.449	0.514	0.519
k- ϵ	-	-	-	0.49	-	0.502
RSM	-	-	-	-	-	0.412
LES	-	-	-	-	-	0.456

Table 7.3: Swirl number at $\frac{x}{D} = -0.8$ from the combustion chamber opening.

7.2 Results with Different Meshes

Different meshes were used in the simulations, refer to chapter 5 for a description of the different meshes. To compare these meshes, simulations were done in CFX with the SST model. There is a significant difference which can be seen in figure 7.2 and also in the different swirl number tables. The mesh called 'mix mesh 1' shows larger variations in concentration in all evaluation planes. The difference between the tetrahedral mesh and the better of the mixed meshes is most evident at the centre.

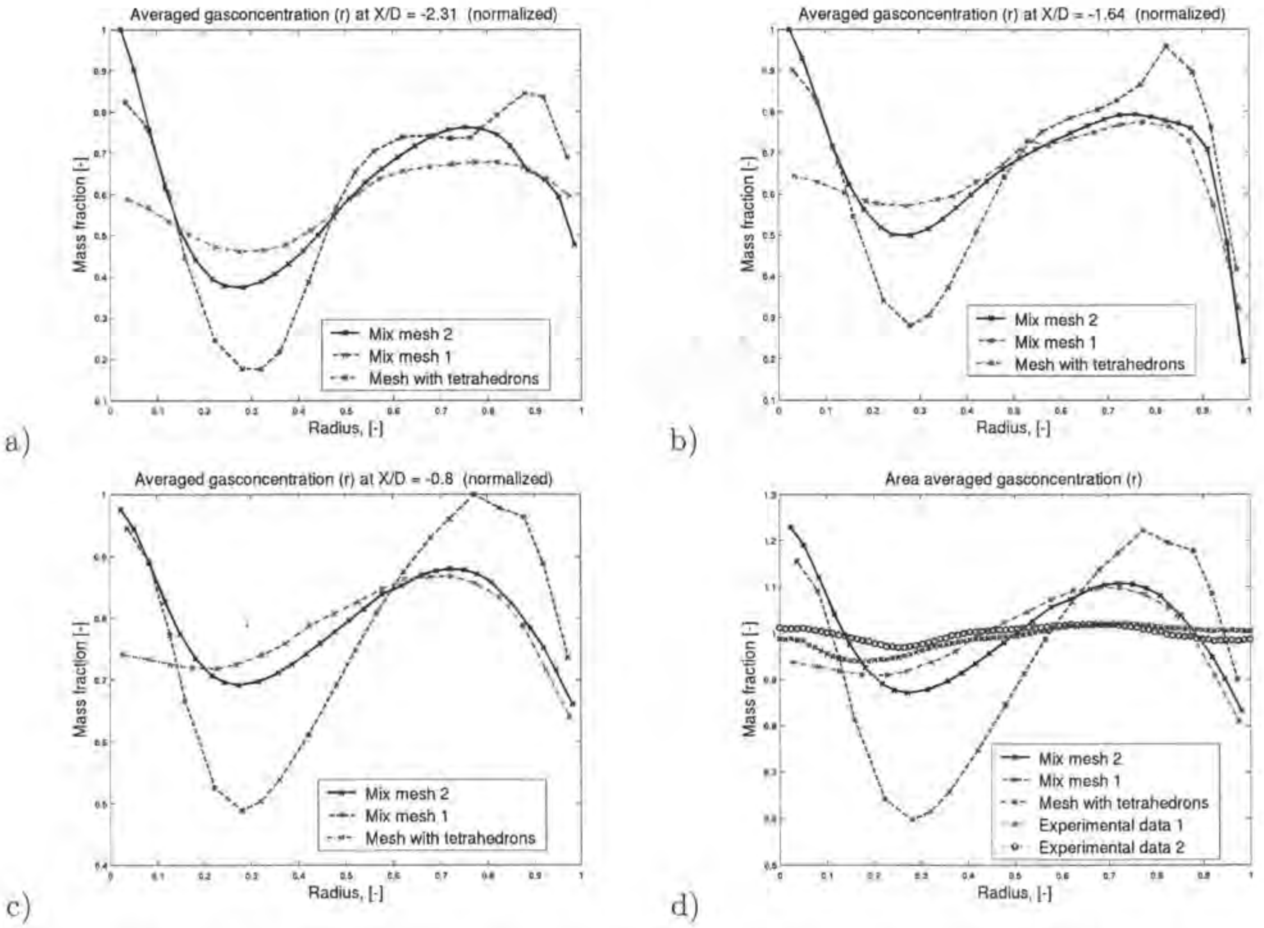

Figure 7.2: CFX simulations with mix mesh 2(black), mix mesh 1(red) and tet mesh(magenta). The simulations are also compared to experimental values(blue).

In figures 7.3 and 7.4 the mass fraction and the axial velocity along the centre lines have been plotted. From them it can be seen that the tetrahedral mesh largely overshoots the central recirculation zone.

From the results in figure 7.2 d one could say that the tetrahedral mesh is better because the results are closer to the experimental data. However, after seeing the large difference in recirculation zone in figure 7.3, this view must be criticised. The recirculation zone should be at the burner outlet at $\frac{x}{D} = 0$. If this means that the flow field is inaccurate with the tetrahedral mesh, the mass distribution can not be correct. The only way to have an accurate mass distribution from an inaccurate flow field is to make more mistakes to compensate for the first mistakes.

7.3 Results with Different CFD Codes

Both CFX and OpenFOAM were used for simulations with the SST model, 'mix mesh 2' and first order upwind. In figure 7.5 and 7.6 the results of the scalar distribution is visible for both CFX and OpenFOAM. It can be seen that resemblance between the two different codes is good for all three planes.

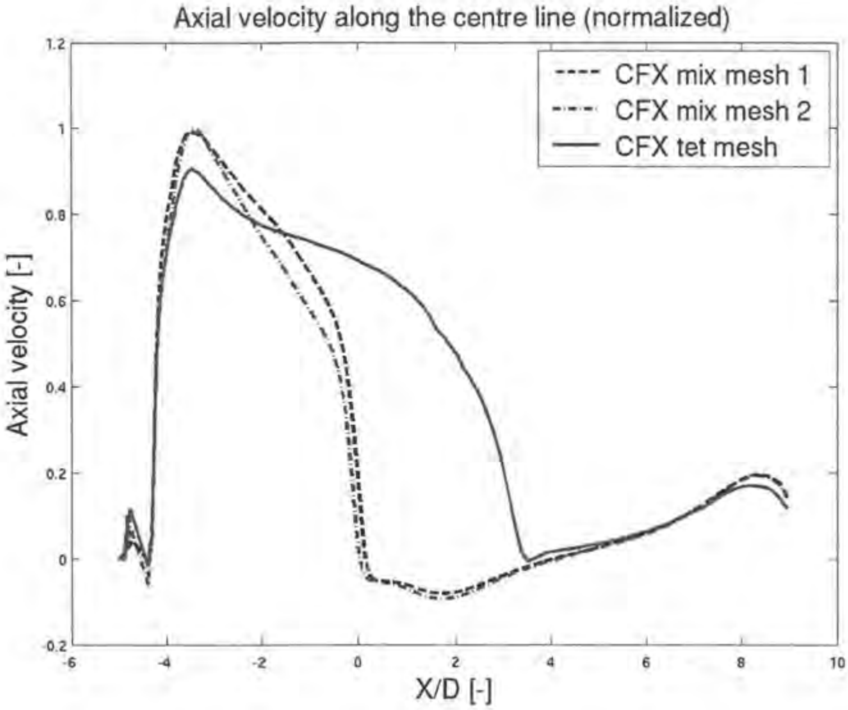

Figure 7.3: Axial velocity for different meshes along the centre line.

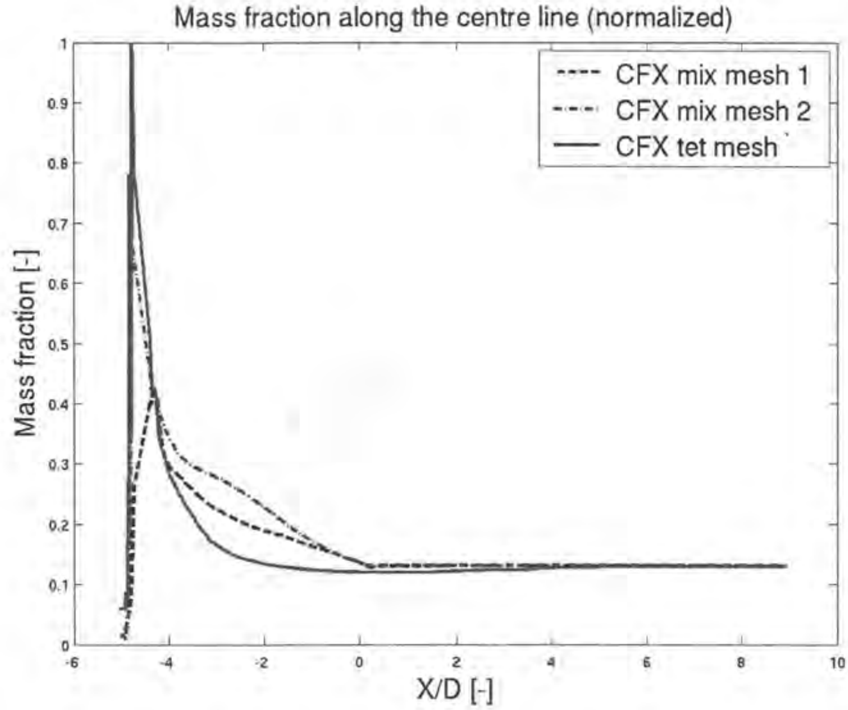

Figure 7.4: Mass fraction for different meshes along the centre line.

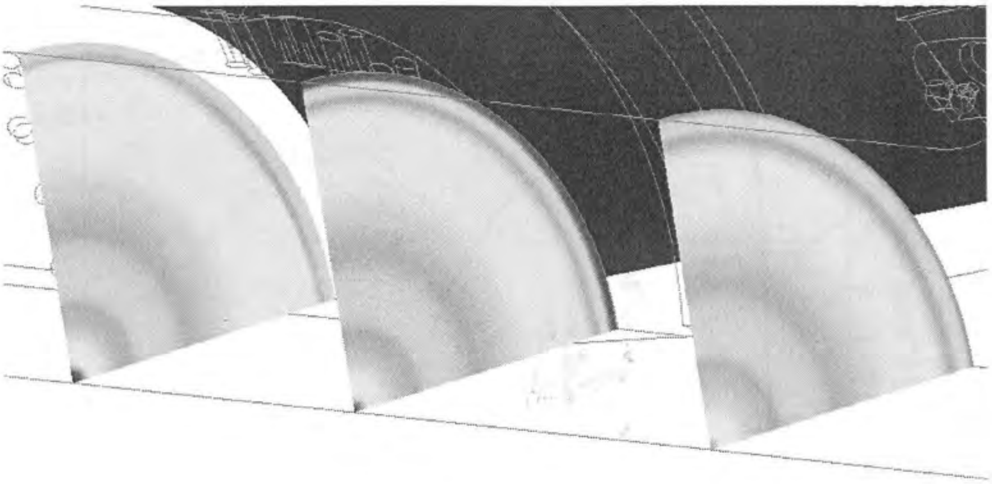

Figure 7.5: Scalar concentration at the three planes using OpenFOAM.

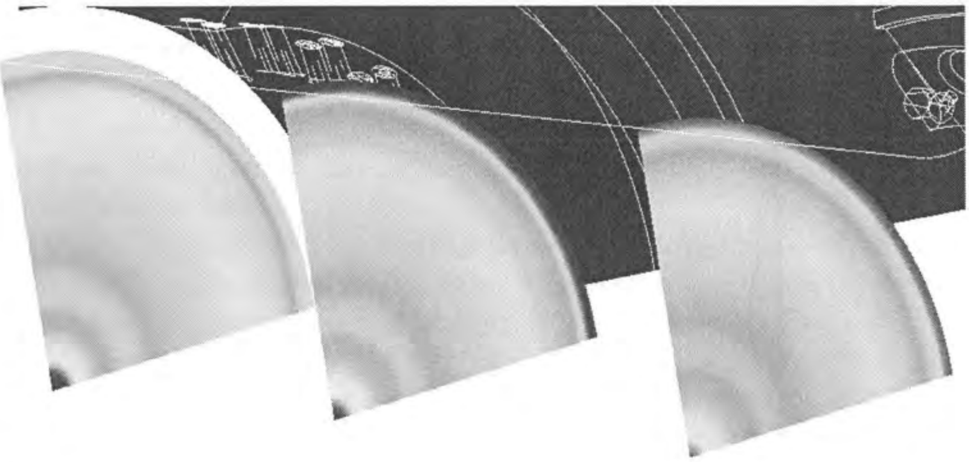

Figure 7.6: Scalar concentration at the three planes using CFX.

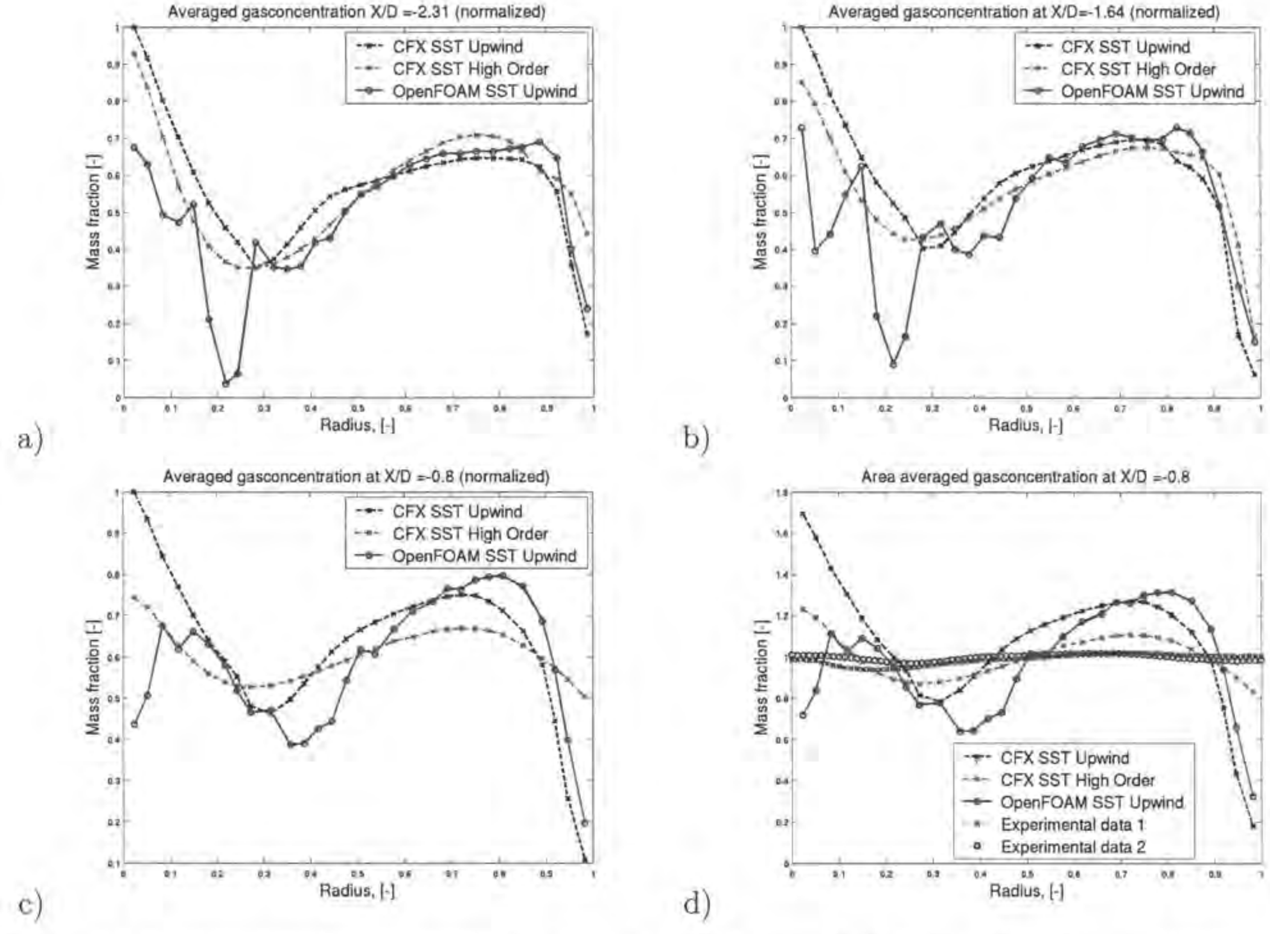

Figure 7.7: Mass fraction averaged at constant radius from CFX first order scheme(black), CFX high order scheme(magenta) and OpenFOAM(red). The simulations are also compared to experimental values(blue).

There is a large difference between the codes at the centre line. Figure 7.8 and figure 7.9 show that there are lower values in OpenFOAM at the extreme points for both the scalar concentration and the axial velocity. If the axial velocity in the whole mixing tube, and not just at the centre line, is lower in OpenFOAM, this would explain the higher swirl numbers for OpenFOAM since the axial momentum is found in the swirl number denominator.

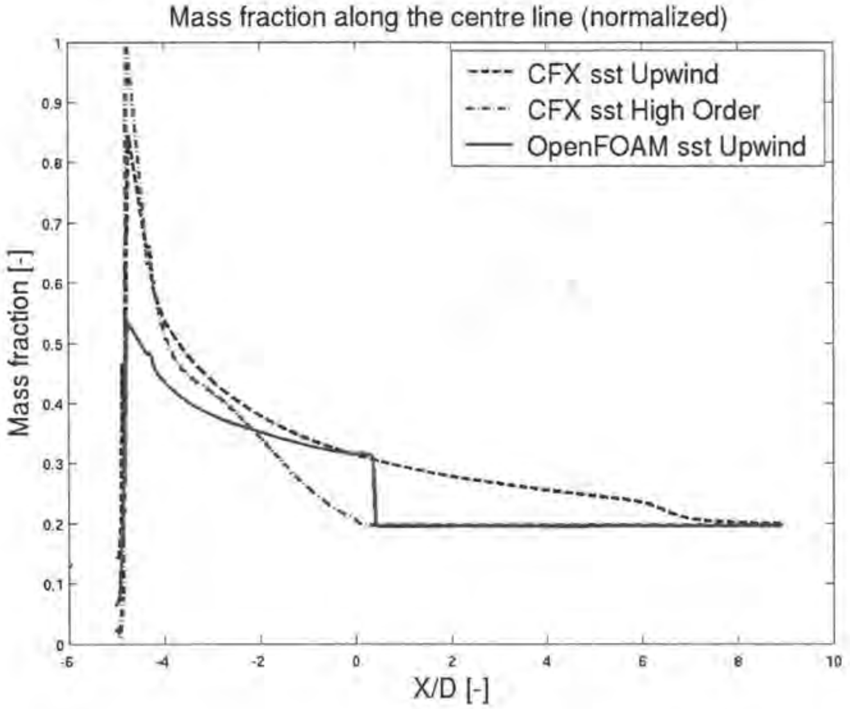

Figure 7.8: Scalar concentration along the centre line using both CFX and OpenFOAM.

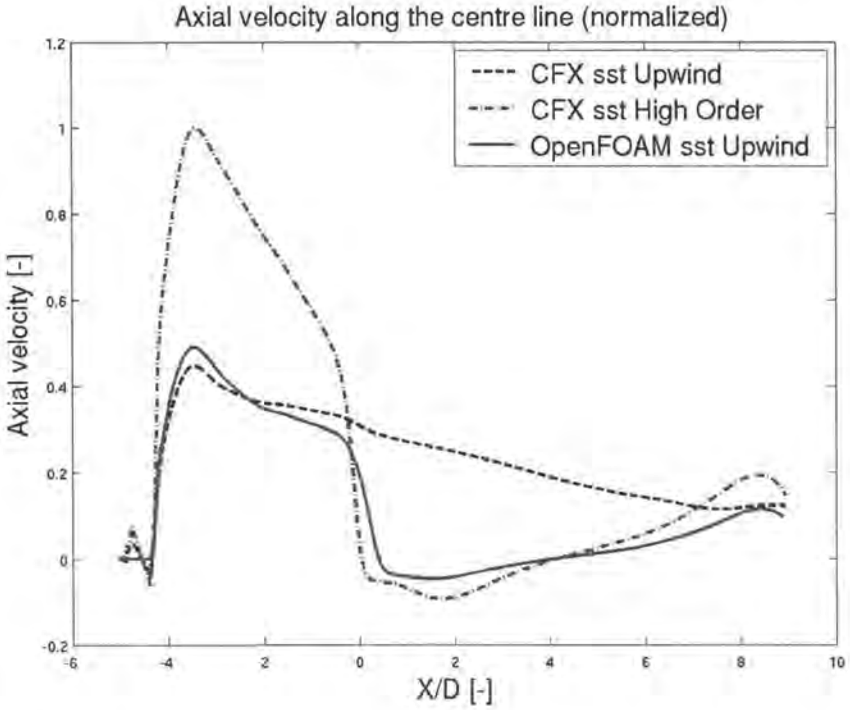

Figure 7.9: Axial velocity along the centre line using both CFX and OpenFOAM.

A plus for OpenFOAM is that even with first order upwind scheme, OpenFOAM catches the recirculation zone at the centre. However, at the same place as the recirculation zone, figure 7.8 shows a sudden drop in mass fraction concentration. The sudden mass fraction drop is between the levels of the both CFX simulations and should therefore be ruled out as unlikely but not unphysical. This is a behaviour that has not been seen in any other simulation and speaks against the OpenFOAM simulation. This sudden drop does suggest a better grid refinement in this area since there is a large gradient.

Another problem with OpenFOAM is the large variations in swirl number. But since this is also the case with CFX, the large variations are probably due to the first order scheme.

7.4 Reynolds Averaged Navier- Stokes and Large Eddy Simulations

In figures 7.11 and 7.12 the scalar concentration is shown as surface plots. It can be seen that the SST model is no way near the level of detail as the LES model displays. A plot of the pressure at some of the gas inlets is also shown in figure 7.10. In the figure it can be seen that there are large variations of the pressure, which means that the inflow through the different gas inlets should vary in mass flow. This was not allowed in the simulation as a fixed velocity inlet were used at all the different holes.

Also it must be said that the sampling time was very short. During the sampling time, the fluid should at least be allowed to pass from the gas injection to the burner outlet at $\frac{x}{D} = 0$. If this criteria is used, the sampling time should be at least three times as long. Even then the sampling time can be to short. The fluctuations should be allowed to vary over a few periods when averages are made.

With these issues, gas inlet pressures and sampling time, the LES simulation is not correct and precautions must be taken when evaluating results. The LES could work as a sign post showing the direction but no definitive conclusions should be drawn.

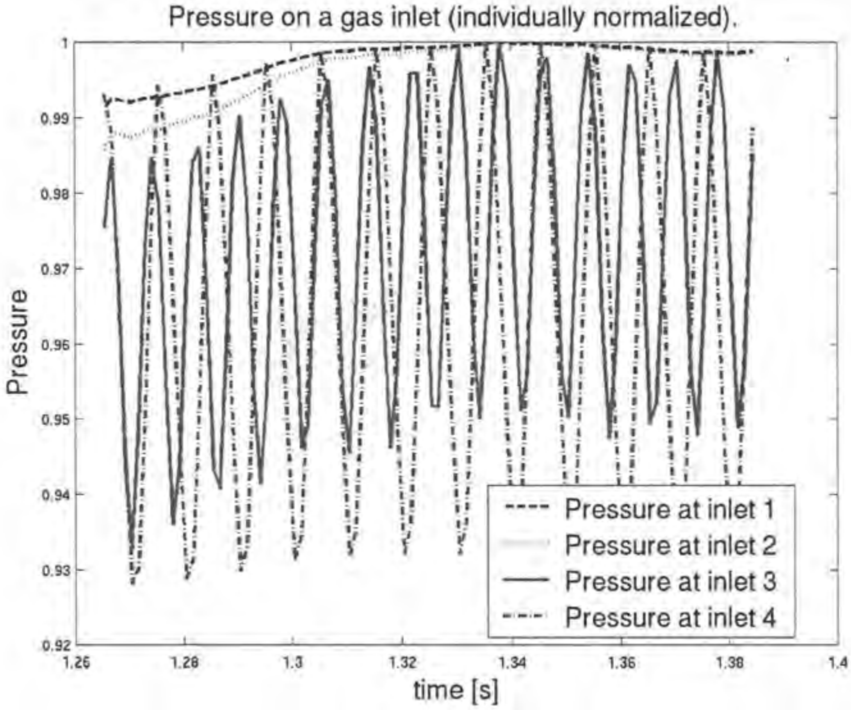

Figure 7.10: Pressure at four of the gas inlets.

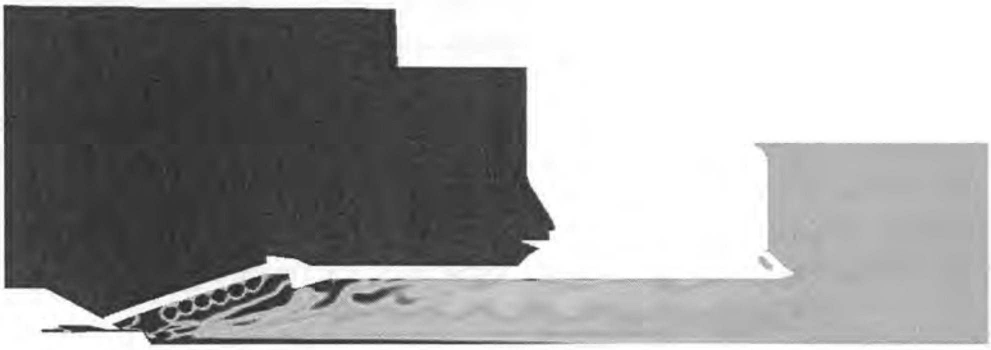

Figure 7.11: Scalar concentration from CFX with mix mesh 2 and SST model.

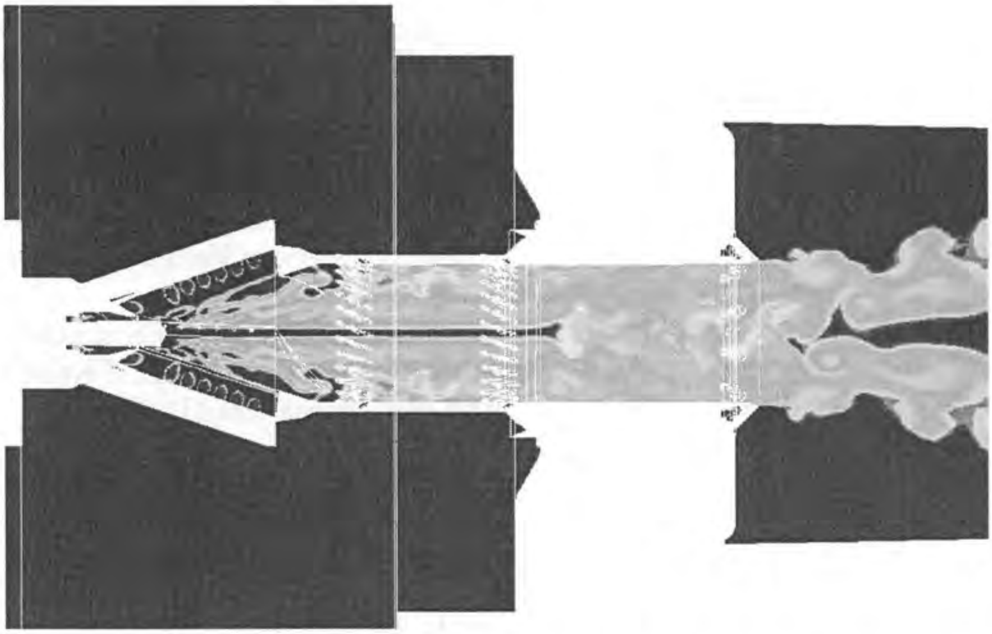

Figure 7.12: Scalar concentration from CFX with mix mesh 2 and LES model.

Some words about the results from the LES simulation (or sign post) then. As visible in the swirl number tables in section 7.1, the swirl number for the LES simulations show some different behaviour than the RANS simulations. Between the first and second evaluation planes, there is a decrease in the LES swirl number where the RANS simulations show an increase.

In figure 7.13, the mass fraction for the different planes can be seen. The results from the SST model are compared with the root mean square (rms) value of the LES simulation. At the first two evaluation planes, at $\frac{x}{D} = -2.31$ and $\frac{x}{D} = -1.64$, the two different plots fit each other reasonably good but in 7.13 c, the LES plot show distinct differences from the SST simulation. Judging from figure B.20 b, this means that the LES simulation was not fully developed at $\frac{x}{D} = -0.8$ when the data was sampled. When the LES simulation runs long enough, as in the first two planes, the results point towards a good agreement with the RANS models.

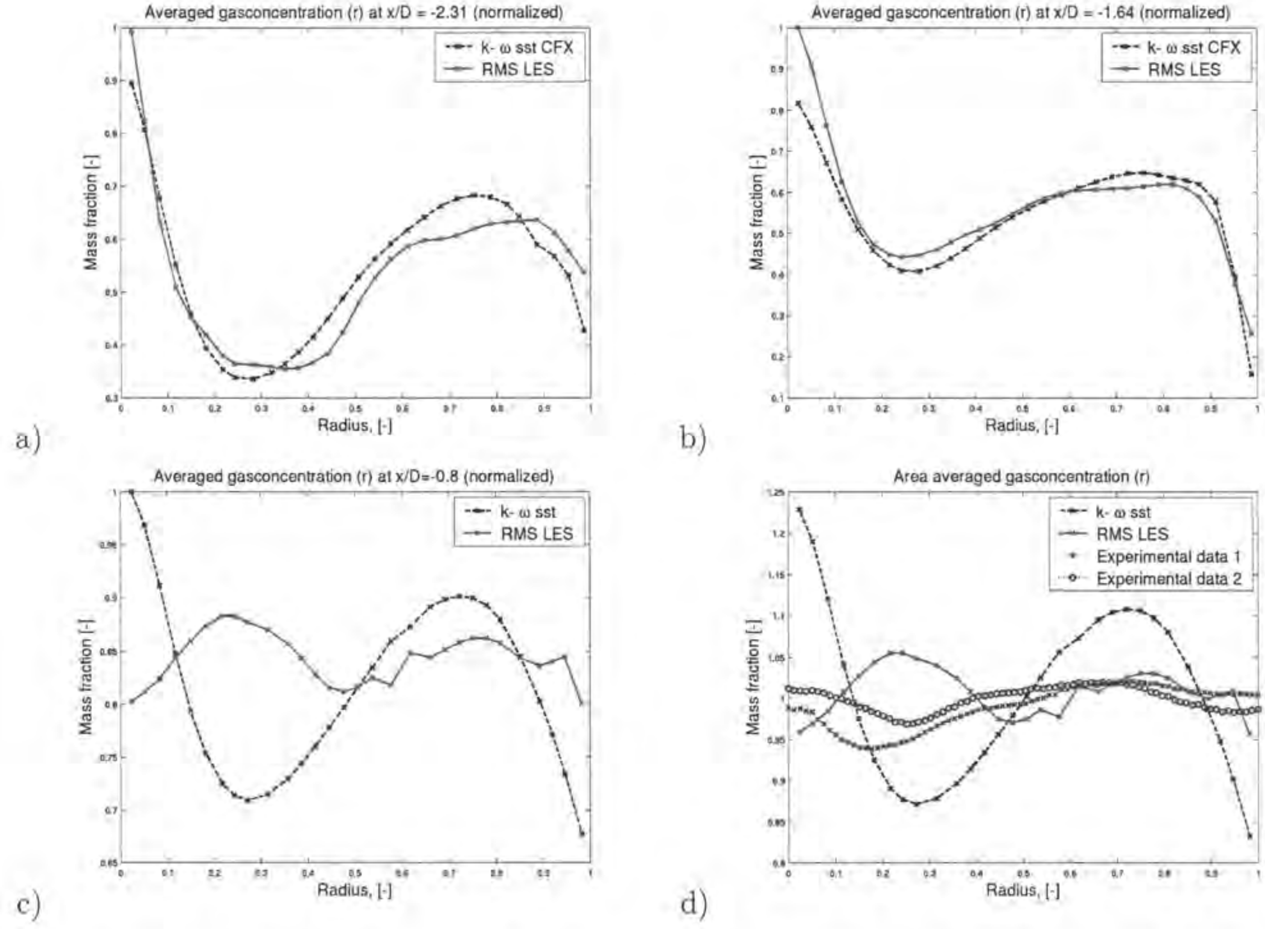

Figure 7.13: Mass fraction averaged at constant radius from CFX SST(black) and root mean square(RMS) from LES(magenta). The simulations are also compared to experimental values(blue).

7.5 Experimental Data and Simulations

The results from the simulations have been compared to the experimental data. The comparison can be seen in figures 7.2 d, 7.7 d and 7.13 d. They show that neither CFX nor OpenFOAM predicts the experiments well using any steady state RANS model. This is not surprising since the experimental results are time averaged. An unsteady RANS simulation could predict the experimental data better.

When LES is used on the other hand, figure 7.13 d shows that the results are closer to the experimental data. But, as discussed in section 7.4, these results should not be trusted until the LES simulation has been completed. Other results from the same LES simulation show rather that the LES simulation will be more in line with the earlier RANS methods and not the experimental data. If this is the case there is little hope that an unsteady RANS simulation should show different results.

8 Conclusions

OpenFOAM has with some difficulty been able to reproduce the results of the commercial software CFX in the test case. as well as for the gas turbine burner simulations. The main difficulty was the unexpected Schmidt number which also was the reason for the creation of the test case.

It can be seen in B.9 and B.10 that out of the RANS models that were used for simulations, the $k-\epsilon$ model works best. This says more about steady state RANS simulations in general for this case and not so much about the $k-\epsilon$ model. It can be seen in figures B.19 a and b that the $k-\epsilon$ model does not show the same level of detail as the other RANS models that were used. This means that the $k-\epsilon$ model could not capture any of the fluctuations that creates higher local concentrations of fuel in the burner. This higher fuel concentration is part of creating the problems that were described in section 1.6.

The more difficult question to answer regarding OpenFOAM is, how much development is needed before OpenFOAM is fully capable to simulate the flow in a gas turbine burner. There are a few error sources that needs to be pointed out. Of course the knowledge and ability of the author is limited. Secondly, an early version of the rotationally periodic general grid interface was used. Even with these two error sources considered the question still remains, how much more development work is needed before OpenFOAM is able to simulate flows as good as the commercial code.

It can also be seen in both the test case and the burner simulations that the mesh has a strong influence on the solution.

9 Future work

A lot more can be done to validate the performance of OpenFOAM. One question raised during the work is how OpenFOAM handles different meshes in terms of cell quality. Further work can be done to find out if OpenFOAM is better or worse then other codes at handling bad cells in terms of cell skewness or volume ratios between neighbouring cells.

Further investigations can also be made by using unsteady RANS models and LES in OpenFOAM. This should give answers about the flow in the burner. An accurately simulated flow, is of course the basis of simulating the gas distribution accurately, but it is not enough.

To accurately solve the scalar distribution to simulate the gas distribution, more investigations should be made about the Schmidt number used in the scalar distribution equation. The test case in chapter 6 leaves many questions to answer. Not only about the differences between CFX and OpenFOAM, but also how close both of them simulate the reality.

References

[1] L. Davidson. MTF270 turbulence modelling. Lecture notes, www.tfd.chalmers.se/doct/comp_turb_model/, Dept. of Thermo and Fluid Dynamics, Chalmers University of Technology, Göteborg, Sweden, 2008.

[2] Peyman Mohammdi and Anders Arato. Dle burner water rig simulations. Bachelor report MDH.IDT.FLYG.0187.2008.GN300.15HP.E, Department of Computer Science and Electronics, Mälardalen University, 2008.

[3] OpenFOAM Forum. Openfoam forum. `http://www.cfd-online.com/Forums/openfoam/`, 2009. retrieved 2009-05-18.

[4] OpenFOAM Wiki. Openfoam wiki. `http://openfoamwiki.net`, 2009. retrieved 2009-05-18.

[5] Siemens AG. Siemens ag. `http://www.powergeneration.siemens.com/products-solutions-services/products-packages/`, 2009. retrieved 2009-05-18.

[6] H.K. Versteeg and W. Malalasekera. *An Introduction to Computational Fluid Dynamics - The Finite Volume Method.* Pearson Education Limited, Harlow, England, 1995.

[7] D.C. Wilcox. *Turbulence Modeling for CFD.* DCW Industries, Inc., 5354 Palm Drive, La Cañada, California 91011, 1993.

A OpenFOAM

A.1 Guidelines

In this section some guide lines on how to use OpenFOAM are presented. The guide lines are a summary of the experience gained during the thesis project. The aim of this section is not to present a complete picture on how to use all utilities and solvers that are used in the project, only to briefly describe what have been learnt about OpenFOAM. More characteristics of OpenFOAM are described in 3.1. The OpenFOAM version that was used in this work is the 1.5-development version.

A.1.1 Mesh generation

During the project, only the *fluent3DMeshToFoam* utility is used. The mesh in question needs to be in ASCII format.

After importing the mesh, the boundary file, *constant/polyMesh/boundary*, needs to be edited. All part identification(PID) names are imported with the mesh. In this thesis work three different settings have been used for different parts of the boundary. For walls *type wall;* were used and *type patch;* were used for all inlets and outlets. The rotationally periodic general grid interface boundaries were defined with

```
    Periodic_Right
    {
        type cyclicGgi;
separationOffset (0 0 0);
rotationAxis (1 0 0);
rotationAngle -90;
shadowPatch Periodic_Left;
        nFaces          24449;
        startFace       4930546;
    }

    Periodic_Left
    {
        type cyclicGgi;
separationOffset (0 0 0);
rotationAxis (1 0 0);
rotationAngle 90;
shadowPatch Periodic_Right;
        nFaces          24449;
        startFace       4976721;
    }
```

The number of faces on the given boundary, *nFaces* and the start face, *startFace*, were given for all boundaries when the mesh is imported.

A.1.2 Case setup

The input files that the case requires needs to be edited or created. If an input file does not exist, OpenFOAM will politely tell in terms of an error message, which file is missing. Such an error message is not difficult to understand and the user should read all error messages. E.g., the error message

```
cannot open file

file: .../0/U at line 0.

     From function regIOobject::readStream(const word\&)
    in file db/regIOobject/regIOobjectRead.C at line 66.

 FOAM exiting
```

means that there is no file 'U' (usually the velocity field) in the folder for initial values and boundary conditions ('0'). To create such a file, the pattern from one of the velocity input files in a tutorial can be followed.

The files for the initial and boundary conditions are all gathered in the '0' directory. For each variable, the boundary condition for all boundaries specified in *constant/polyMesh/boundary*, are given. There are a wide variety of boundary conditions to choose from.

A.1.3 Processing

During the work a standard OpenFOAM solver called *simpleFoam* were used. This solver was expanded to include scalar transport by adding

```
solve
  (
          fvm::div(phi, c)
        - fvm::laplacian((turbulence->nuEff())/Sc, c)
  );
```

to the existing solver. The Schmidt number was set in *constant/transportProperties* as the already existing viscosity *nu* is set. This means that some lines of codes had to be added to the file *createFields.H* so that the given Schmidt number and initial scalar field, c, are read by the solver.

The *simpleFoam* solver is based on the simple algorithm. For details on this algorithm, refer to a CFD text book, such as [6].

When using the solver, the results should be stored in a log file. This is achieved by executing with

```
mySolver > myLogFile
```

There is a utility, *foamLog*, that extracts the values in the log file. The information that is found in the log file are all the information, OpenFOAM is told to write in the command window during run. Among the default settings are residuals and number of sub iterations.

A.1.4 Post processing

The post processing of OpenFOAM simulations in this thesis was made in CFX. To export the result there are a number of utilities to use that will transform the data to the correct format. The utility that were used in this thesis was *foamMeshToFluent* and *foamDataToFluent*. To use them there needs to be a file, *foamDataToFluentDict*. This file can be found in the OpenFOAM installation at *applications/utilities/postProcessing/dataConversion/foamDataToFluent/*.

A.2 OpenFOAM Solvers

Attempts were made to use other solvers in OpenFOAM, one of them was *reactingFoam*. The attractive feature of this solver is the ability to use different substances. The idea to use two substances with the properties of water and to track the mixing between them failed. The case setup was not as easy as believed and this idea was a dead end.

Also, the solver *simpleBuoyantFoam* was used. This time the inlets would be given different temperatures. However, a suitible way of handling the thermodynamic properties could not be found.

B Results

In this appendix, more results are presented.

B.1 Swirl Number Numerator

The swirl number numerator as defined in equation 7.1. The result is presented in tables B.1 - B.3

	OpenFOAM			CFX		
	tet mesh	mix mesh 1	mix mesh2	tet mesh	mix mesh 1	mix mesh2
SST First order scheme	-	-	$4.93 \cdot 10^{-4}$	-	-	$5.03 \cdot 10^{-4}$
SST High order scheme	-	-	-	$3.88 \cdot 10^{-4}$	$4.03 \cdot 10^{-4}$	$6.12 \cdot 10^{-4}$
k- ϵ	-	-	-	$3.87 \cdot 10^{-4}$	-	$5.7 \cdot 10^{-4}$
RSM	-	-	-	-	-	$5.08 \cdot 10^{-4}$
LES	-	-	-	-	-	$5.72 \cdot 10^{-4}$

Table B.1: Swirl number numerator at $\frac{x}{D} = -2.31$ from the combustion chamber opening.

	OpenFOAM			CFX		
	tet mesh	mix mesh 1	mix mesh2	tet mesh	mix mesh 1	mix mesh2
SST First order scheme	-	-	$4.97 \cdot 10^{-4}$	-	-	$5.08 \cdot 10^{-4}$
SST High order scheme	-	-	-	$3.99 \cdot 10^{-4}$	$4.15 \cdot 10^{-4}$	$6.31 \cdot 10^{-4}$
k- ϵ	-	-	-	$3.97 \cdot 10^{-4}$	-	$5.9 \cdot 10^{-4}$
RSM	-	-	-	-	-	$5.12 \cdot 10^{-4}$
LES	-	-	-	-	-	$5.67 \cdot 10^{-4}$

Table B.2: Swirl number numerator at $\frac{x}{D} = -1.64$ from the combustion chamber opening.

	OpenFOAM			CFX		
	tet mesh	mix mesh 1	mix mesh2	tet mesh	mix mesh 1	mix mesh2
SST First order scheme	-	-	$4.77 \cdot 10^{-4}$	-	-	$4.81 \cdot 10^{-4}$
SST High order scheme	-	-	-	$3.86 \cdot 10^{-4}$	$4.08 \cdot 10^{-4}$	$6.19 \cdot 10^{-4}$
k- ϵ	-	-	-	$3.83 \cdot 10^{-4}$	-	$5.66 \cdot 10^{-4}$
RSM	-	-	-	-	-	$4.76 \cdot 10^{-4}$
LES	-	-	-	-	-	$5.37 \cdot 10^{-4}$

Table B.3: Swirl number numerator at $\frac{x}{D} = -0.8$ from the combustion chamber opening.

B.2 Mass Fraction Distribution

The mass fraction distribution is presented in different figures. First as surface plots and then as diagrams where the mass fraction has been averaged over constant radius. The same three planes as presented in chapter 7 are used for results evaluation. Where applicable, $\frac{x}{D} = -0.8$,the results are compared to experimental results.

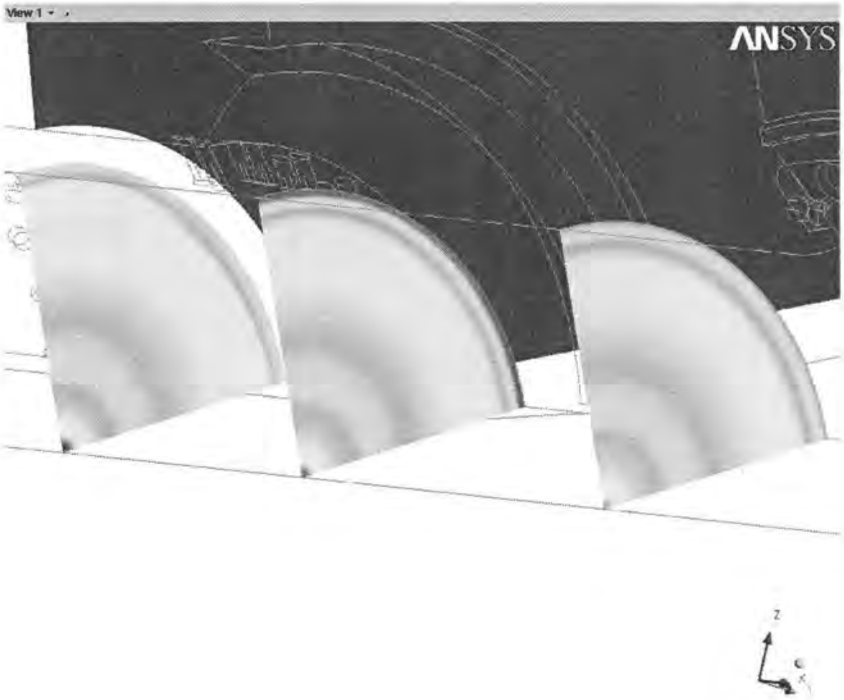

Figure B.1: Scalar concentration at the three planes using OpenFOAM, SST model, mix mesh 2 and first order upwind scheme.

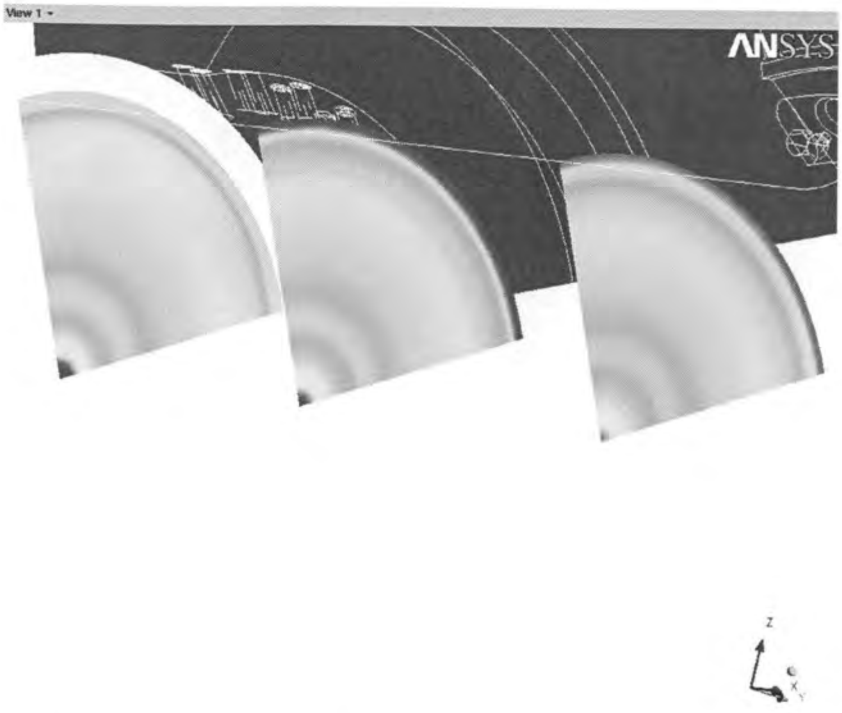

Figure B.2: Scalar concentration at the three planes using CFX, SST model, mix mesh 2 and first order upwind scheme.

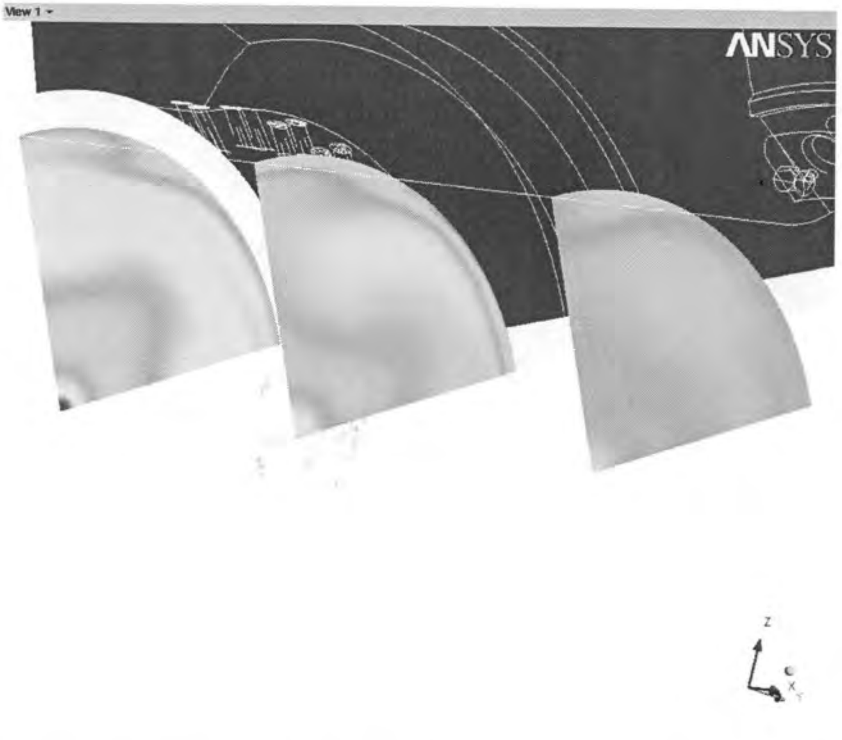

Figure B.3: Scalar concentration at the three planes using CFX, SST model, mix mesh 2 and high resolution scheme.

Figure B.4: Scalar concentration at the three planes using CFX, SST model, mix mesh 1 and high resolution scheme.

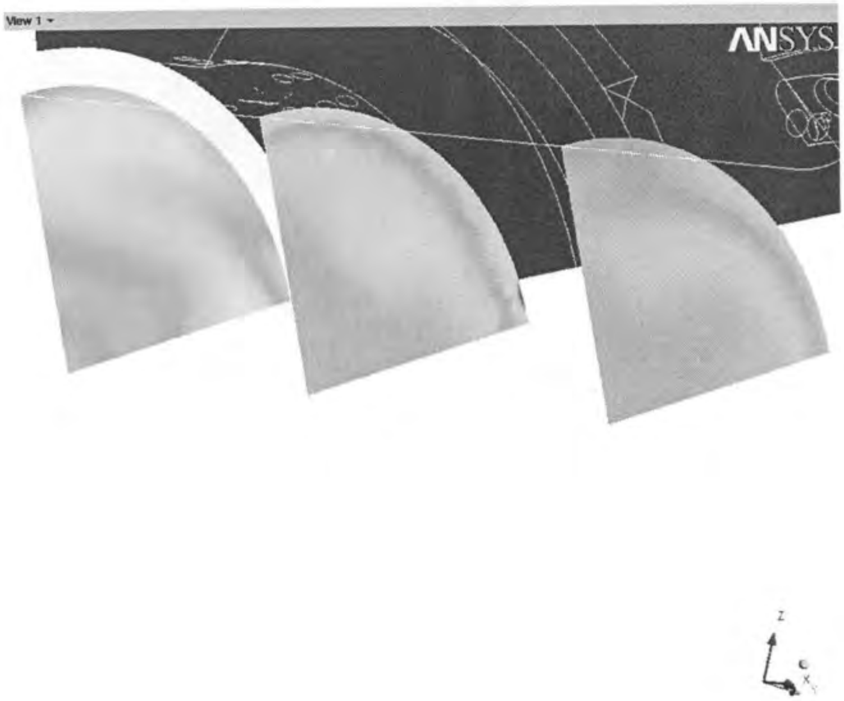

Figure B.5: Scalar concentration at the three planes using CFX, SST model, tet mesh and high resolution scheme.

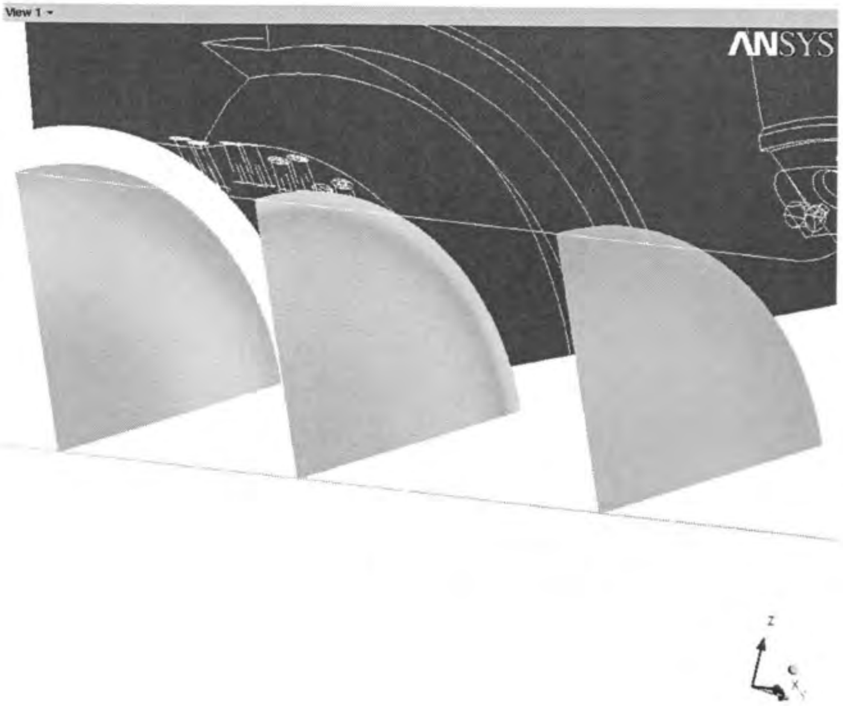

Figure B.6: Scalar concentration at the three planes using CFX, $k - \epsilon$ model, mix mesh 2 and high resolution scheme.

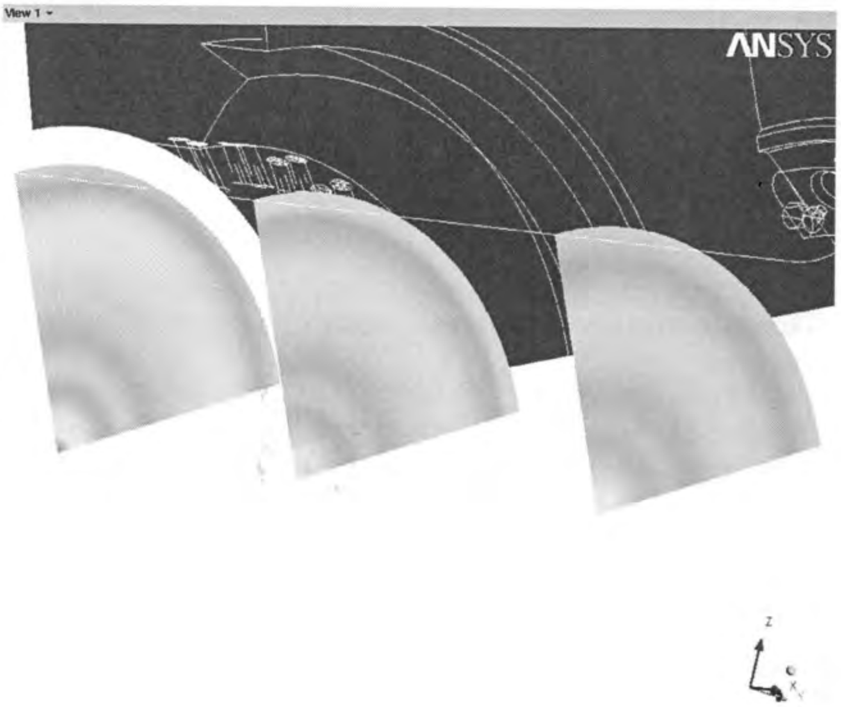

Figure B.7: Scalar concentration at the three planes using CFX, Reynolds stress model, mix mesh 2 and high resolution scheme.

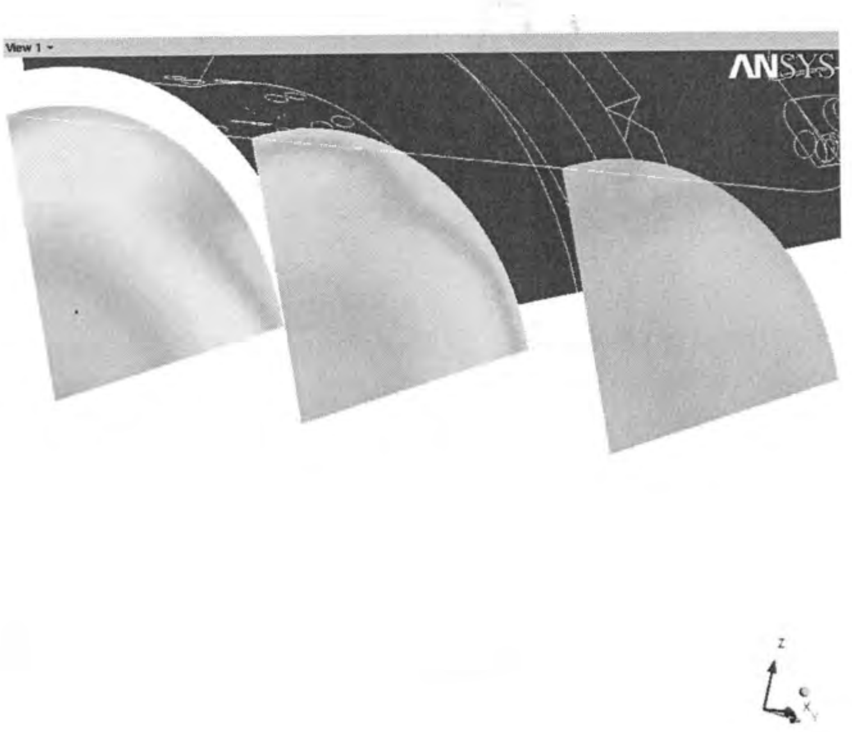

Figure B.8: Scalar concentration at the three planes using CFX, $k-\epsilon$ model, tet mesh and high resolution scheme.

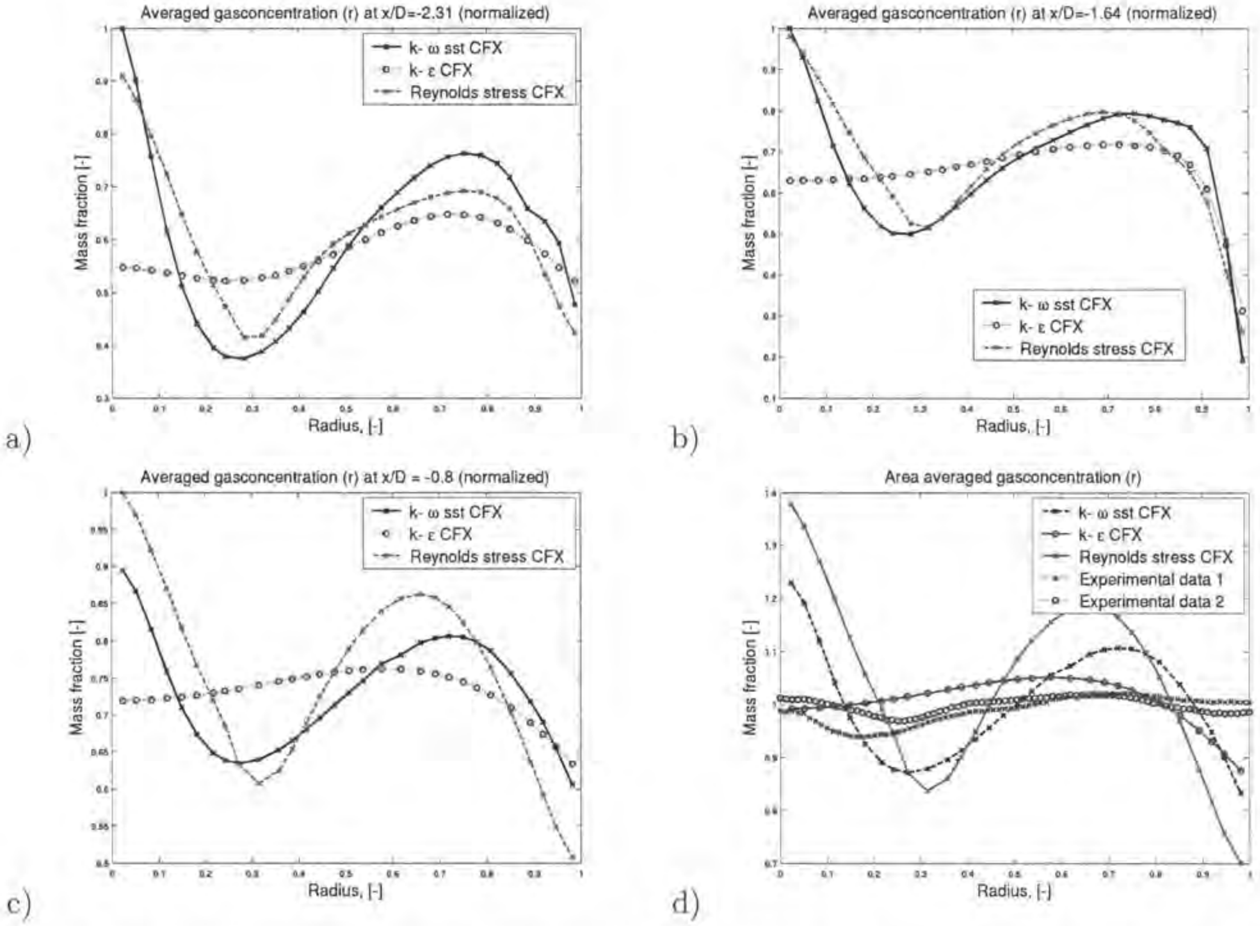

Figure B.9: CFX simulations with SST(black), $k - \epsilon$(red) and Reynolds stress(magenta). The simulations are also compared to experimental values(blue). Mix mesh 2 and high resolution scheme have been used.

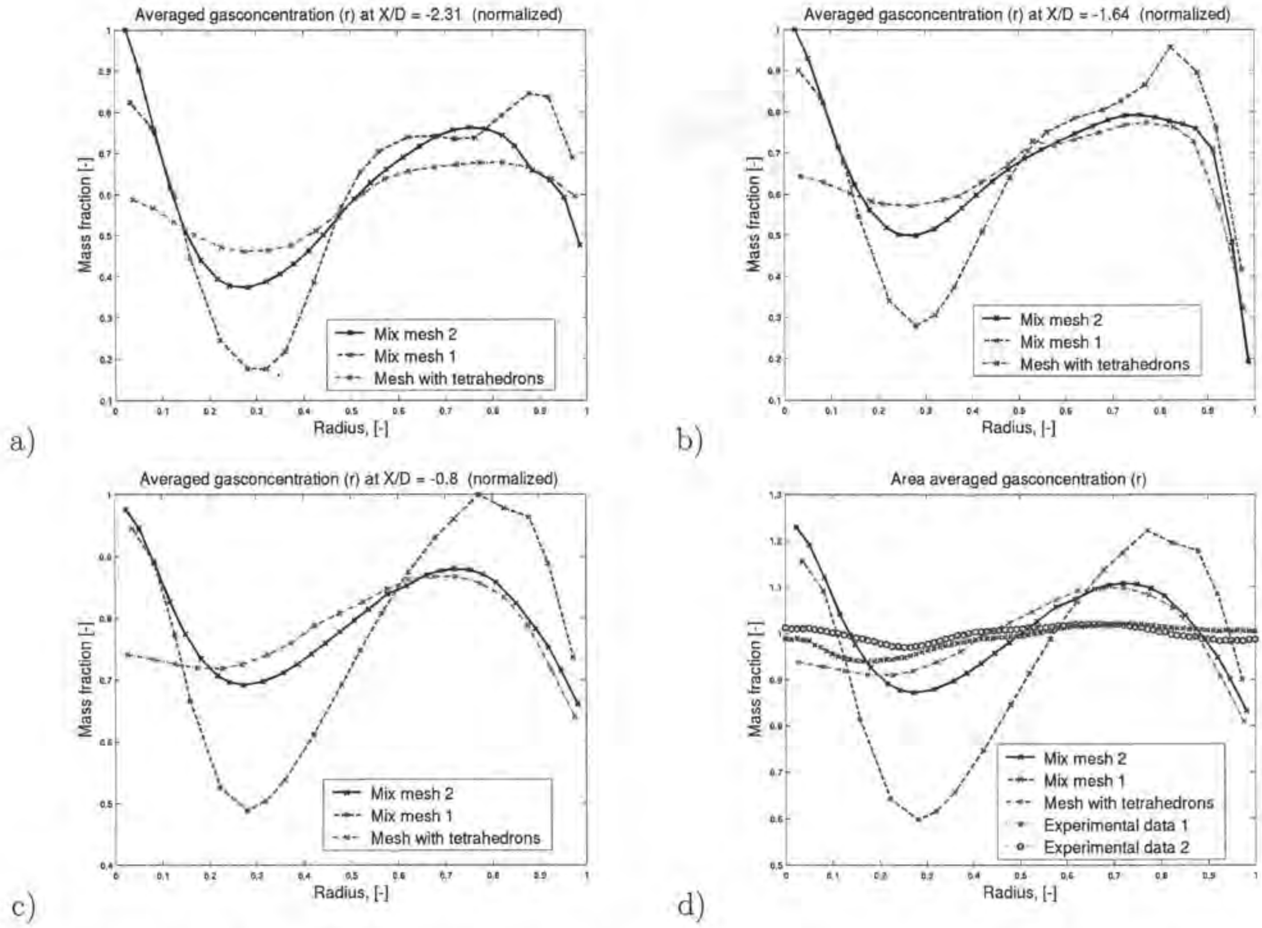

Figure B.10: CFX simulations with mix mesh 2(black), mix mesh 1(red) and tet mesh(magenta). The simulations are also compared to experimental values(blue). SST model and high resolution scheme have been used.

B.3 Velocity Magnitude

The velocity magnitude is presented in different figures. First as surface plots and then as diagrams where the velocity magnitude has been averaged over constant radius. The same three planes as presented in chapter 7 are used for results evaluation.

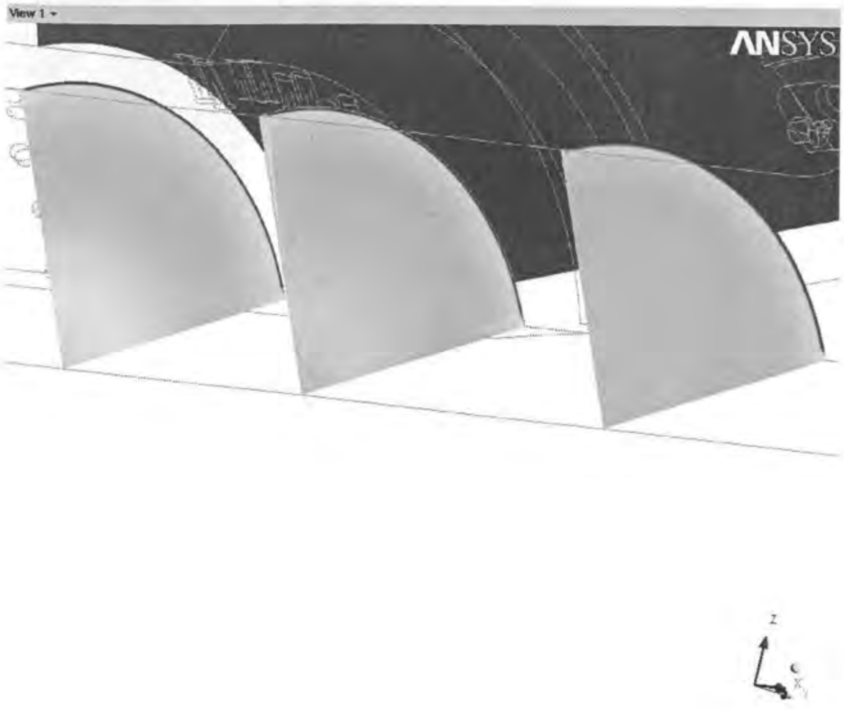

Figure B.11: Velocity magnitude at the three planes using OpenFOAM, SST model, mix mesh 2 and first order upwind scheme.

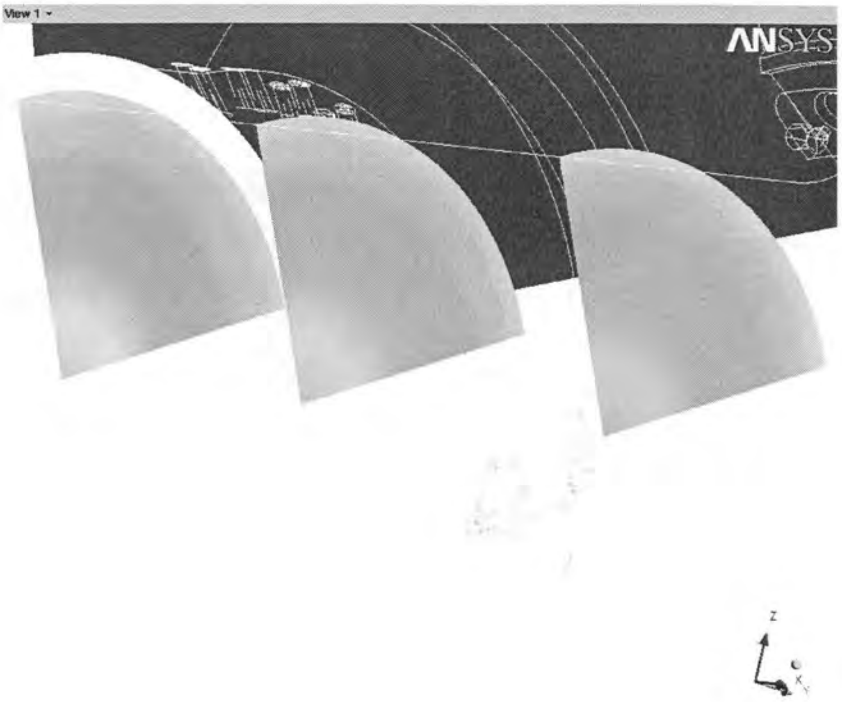

Figure B.12: Velocity magnitude at the three planes using CFX, SST model, mix mesh 2 and first order upwind scheme.

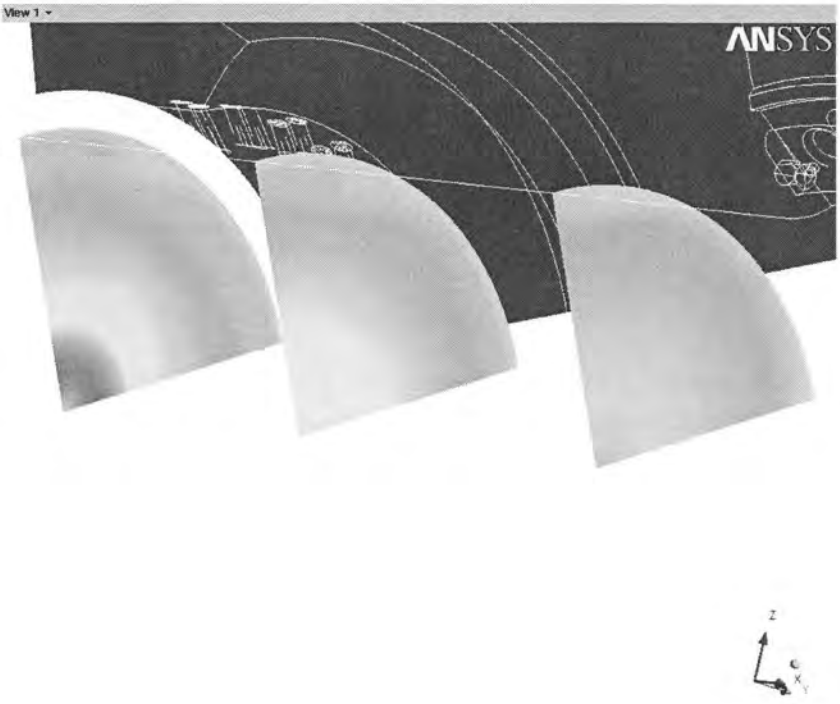

Figure B.13: Velocity magnitude at the three planes using CFX, SST model, mix mesh 2 and high resolution scheme.

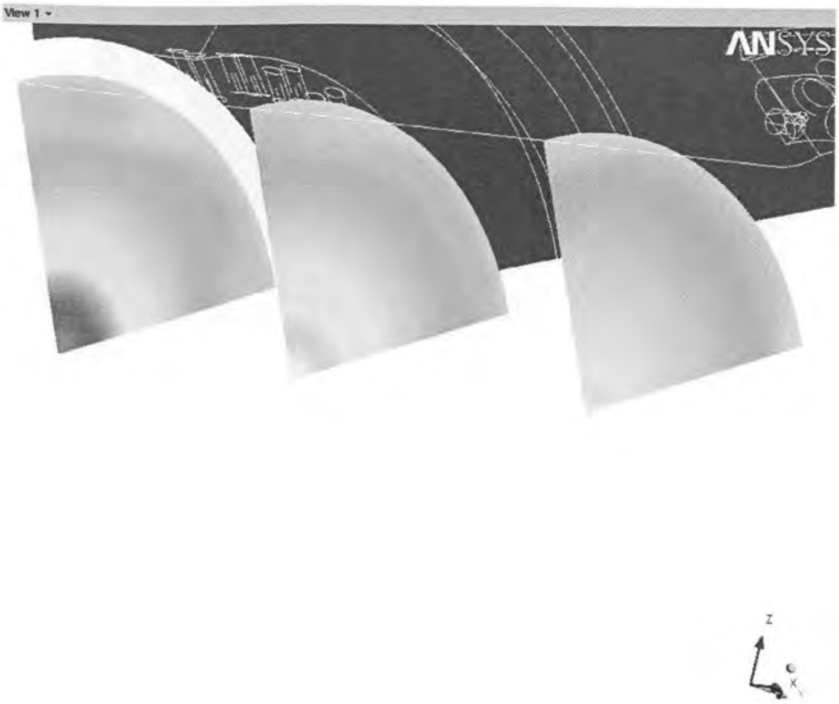

Figure B.14: Velocity magnitude at the three planes using CFX, SST model, mix mesh 1 and high resolution scheme.

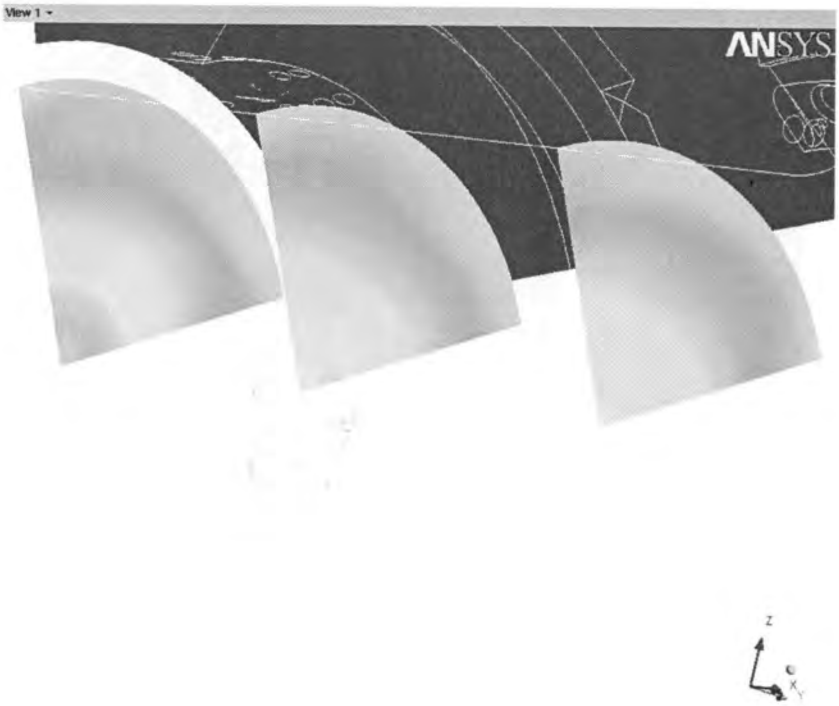

Figure B.15: Velocity magnitude at the three planes using CFX, SST model, tet mesh and high resolution scheme.

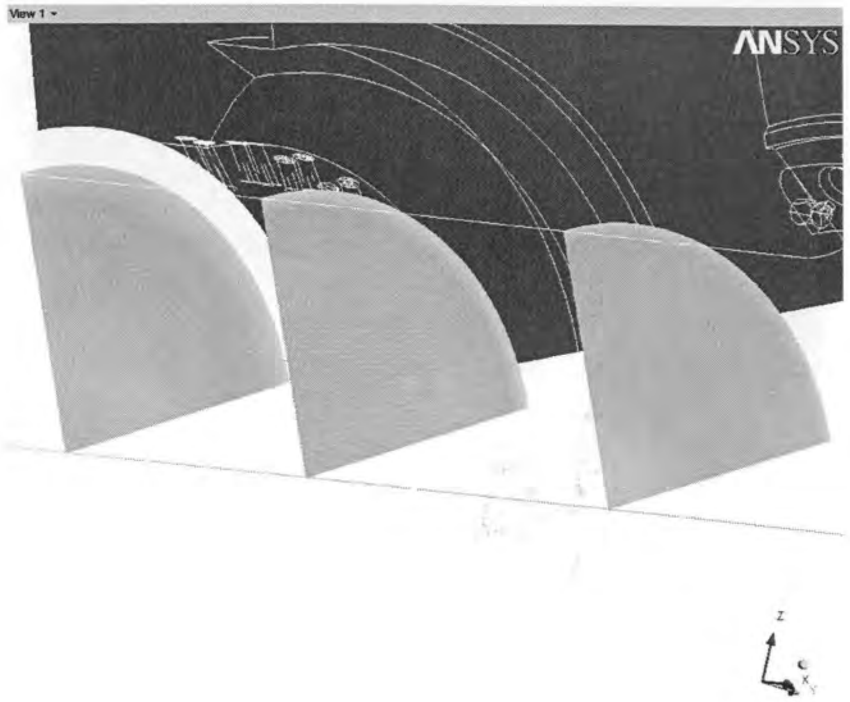

Figure B.16: Velocity magnitude at the three planes using CFX, $k-\epsilon$ model, mix mesh 2 and high resolution scheme.

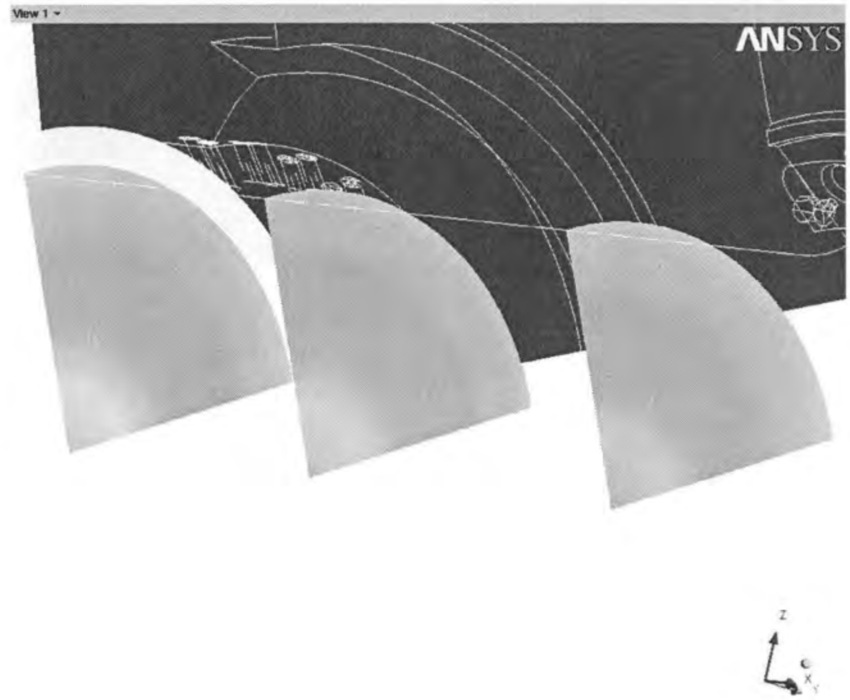

Figure B.17: Velocity magnitude at the three planes using CFX, Reynolds stress model, mix mesh 2 and high resolution scheme.

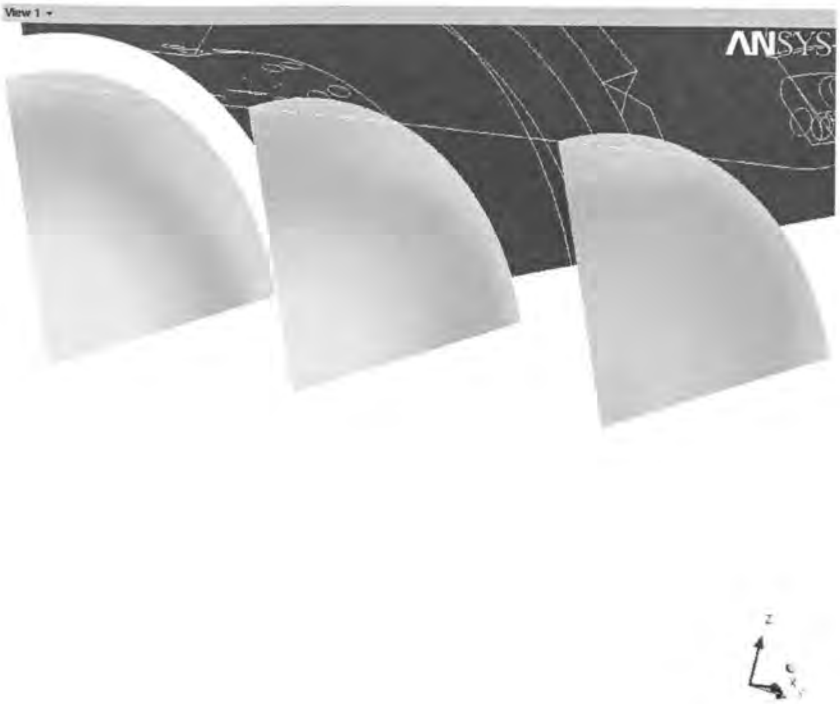

Figure B.18: Velocity magnitude at the three planes using CFX, $k-\epsilon$ model, tet mesh and high resolution scheme.

B.4 Centre Line

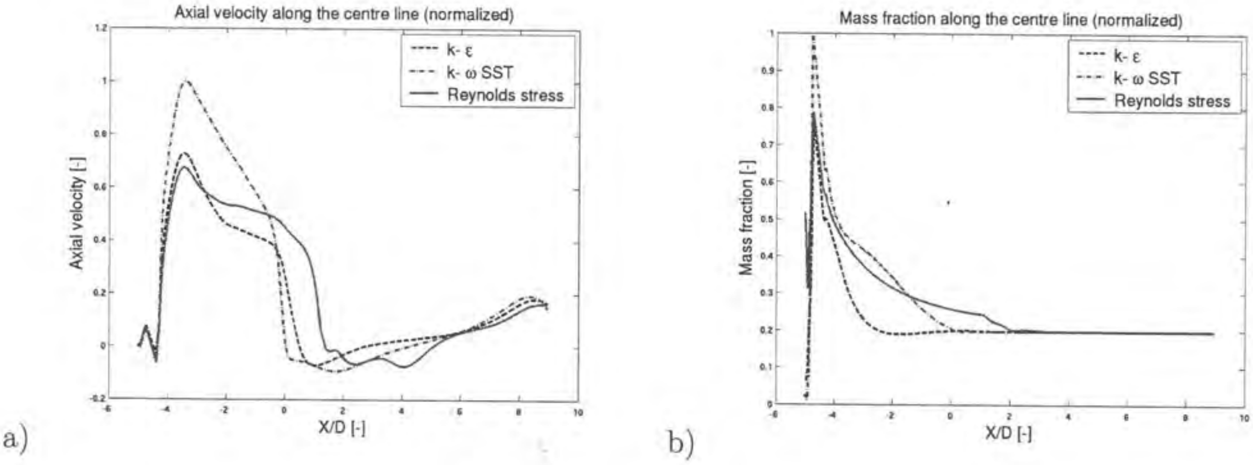

Figure B.19: Axial velocity and mass fraction at the centre line using the $k-\epsilon$ model(black), $k-\omega$ SST model(blue) and the Reynolds stress model(red).

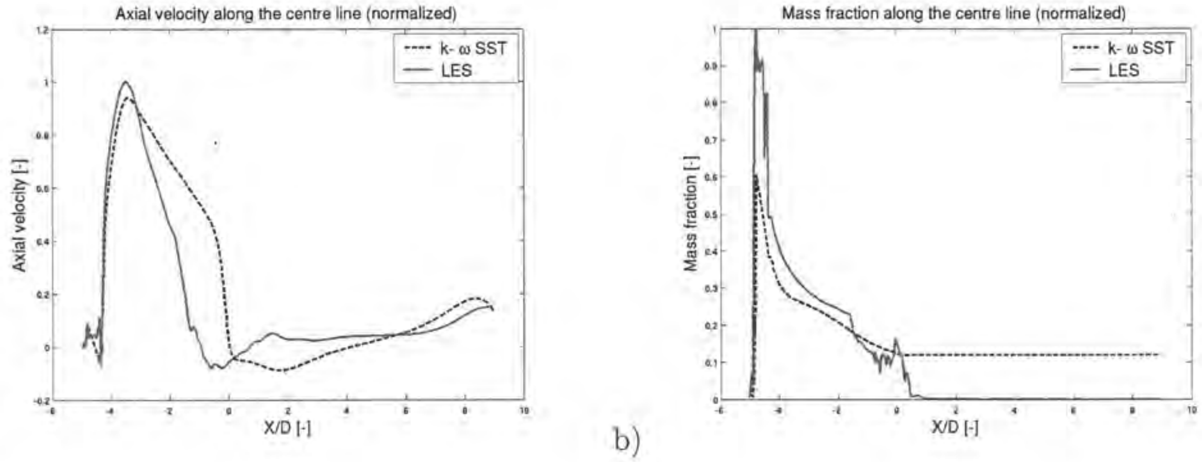

a) b)

Figure B.20: Axial velocity and mass fraction at the centre line using the $k-\omega$ SST model(black) and the LES method(magenta).

CHALMERS UNIVERSITY OF TECHNOLOGY
SE 412 96 Göteborg, Sweden
Phone: + 46 - (0)31 772 10 00
Web: www.chalmers.se